



Photosynthetic electron, carbon and oxygen fluxes within a mosaic of Fe limitation in the California Current Upwelling System

5 Yayla Sezginer¹, Kate Schuler¹, Emily Speciale², Adrian Marchetti², Claire Till³, Ralph Till³, Philippe Tortell^{1,4}

¹Department of Earth Oceans and Atmospheric Sciences, University of British Columbia, Vancouver, BC, Canada

²Earth Marine and Environmental Sciences, University of North Carolina at Chapel Hill, Chapel Hill, NC, USA

³Department of Chemistry, California State Polytechnic University, Humboldt, Arcata, CA, USA

10 ⁴Department of Botany, University of British Columbia, Vancouver, BC, Canada

Correspondence to: Yayla Sezginer (ysezginer@eoas.ubc.ca)

Abstract. We compare primary productivity estimates based on different photosynthetic ‘currencies’ (electrons, O₂ and carbon) collected from the dynamic coastal upwelling waters of the California Current. Fast Repetition Rate Fluorometry and O₂/N₂' measurements were used to collect high-resolution underway estimates of photosynthetic electron transport rates and net community productivity, respectively, alongside on-station ¹⁴C uptake experiments to measure gross carbon fixation rates. Our survey captured two upwelling filaments at Cape Blanco and Cape Mendocino with distinct biogeochemical signatures and iron availabilities, enabling us to examine photosynthetic processes along a natural iron gradient. Significant differences in photo-physiology, cell sizes, Si:NO₃⁻ draw-down ratios, and molecular markers of Fe-stress indicated that phytoplankton assemblages near Cape Mendocino were Fe-stressed, while those near Cape Blanco were Fe-replete. Upwelling of O₂-poor deep water to the surface complicated O₂-based net community productivity estimates, but we were able to correct for these vertical mixing effects using continuous [N₂O] surface measurements and depth-profiles of $\frac{\partial [O_2]}{\partial [N_2O]}$. Vertical mixing corrections were strongly correlated to sea surface temperature, which serves as an N₂O-independent proxy for upwelling. Following vertical mixing corrections, all three productivity estimates reflected trends in Fe-stress physiology, indicating greater productivity near Cape Blanco compared to Cape Mendocino. For all assemblages, carbon fixation varied as a hyperbolic function of electron transport rates, but the derived parameters of this relationship were highly variable and significantly correlated with physiological indicators of Fe-stress (σ_{PSII} , Fv/F_M, Si:NO₃⁻ and diatom-specific PSI gene expression), suggesting that iron availability influenced the coupling between photosynthetic electron transport and subsequent carbon fixation. Net community productivity showed strong coherence with daily-integrated photosynthetic electron transport rates across the entire cruise track, with no apparent relationship with Fe-stress. This result suggests that fluorescence-based estimates of gross photochemistry are still a good indicator for bulk primary productivity, even if Fe-limitation influences the stoichiometric relationship between productivity currencies.



1 Introduction

Along the eastern boundaries of ocean basins, coastal upwelling delivers nutrient-rich deep water to the euphotic zone (Bograd *et al.*, 2023), sustaining high phytoplankton growth rates and primary productivity. Despite representing less than 1% of the 35 surface ocean, these productive upwelling ecosystems, support ~20% of global fishery catches (Pauly and Christensen, 1995), and play a disproportionate role in ocean carbon uptake through the ‘biological carbon pump’ (Mathis *et al.*, 2024). Quantifying rates of primary productivity (PP) within eastern boundary currents is thus vital for accurate carbon budgeting and fishery yield predictions (Marshak and Link, 2021), yet this remains challenging due to the highly dynamic nature of these systems.

The California Current system (CCS) is one of the best studied eastern boundary currents, extending from British Columbia, Canada, to Baja California, Mexico. Upwelling in the CCS occurs during spring and summer when northerly winds drive Ekman transport of surface water offshore. Within the upwelling season, short-term changes in windspeed and direction can dampen or reverse upwelling signals on the scale of hours to days, while complex coastline geometry directs wind flow, 40 creating upwelling hotspots in the lee of capes (Castelao and Luo, 2018). Underlying bathymetric features and deep-water composition further influence the nature of upwelling filaments and the availability of macro and micro nutrients. In regions with shallow and wide continental shelves, sediment deposition provides a primary source Fe and other micronutrients (Deutsch *et al.*, 2021). In contrast, waters overlying steep narrow shelves retain less Fe, and PP in these regions can be limited by Fe availability despite the presence of upwelling conditions (Biller *et al.*, 2013). The resulting ‘mosaic of Fe limitation’ 45 influences the distribution of phytoplankton biomass and productivity across the CCS (Hutchins *et al.*, 1998; Till *et al.*, 2019). Resolving ecosystem responses to such a heterogenous environment requires high resolution measurements.

Traditionally, primary productivity has been measured using discrete bottle incubations where the net change in dissolved O₂ 50 or particulate organic carbon is measured over time. Shorter incubations approximate gross primary productivity (GPP), whereas longer incubations allow time for respiration to act upon tracers, yielding estimates somewhere between GPP and net PP (NPP = GPP – respiration). Although bottle incubations are still widely used to directly observe carbon fixation rates, the 55 resulting measurements can be ambiguous in terms of GPP vs. NPP, while also providing low sampling resolution and posing potential containment artefacts (Banse, 2002). To avoid these challenges, a number of high through-put PP proxies have been developed based on advances in dissolved gas measurements, bio-optical techniques, and satellite-based ocean color 60 observations (Balch *et al.*, 2021). These diverse PP methodologies target different photosynthetic processes, from subcellular light absorption to ecosystem scale carbon export.

At the smallest spatial and temporal scales, Photosystem II (PSII) electron transport rates (ETR_{PSII}) quantify light absorption 65 and conversion to chemical energy for a variety of metabolic activities including carbon fixation. Measurements of ETR_{PSII} can be obtained from active chlorophyll fluorescence techniques, which exploit the inverse relationship between PSII 70 fluorescence and photochemical yields to enable non-invasive and high-frequency measurement from underway seawater lines (Kranz *et al.*, 2020; Sezginer *et al.*, 2023) or autonomous platforms (e.g. Carvalho *et al.*, 2020). Downstream of ETR_{PSII}, carbon fixation can be directly measured using bottle incubations, or approximated from empirical algorithms relating NPP to 75 remotely sensed Chlorophyll (Chl) concentration, sea surface temperature (SST), and photosynthetically available radiance (PAR) (Behrenfeld and Falkowski, 1997; Behrenfeld *et al.*, 2005; Saba *et al.*, 2011). Finally, net community productivity (NCP), represents the difference between GPP and community respiration and can be equated to carbon export out of the mixed layer. This term can be derived from measurements of biological oxygen saturation, ΔO₂/Ar, using Ar-normalization of O₂ to correct for physical influences on gas disequilibria (e.g. temperature or salinity changes or bubble injection) to isolate the biological signal (Craig and Hayward, 1987; Cassar *et al.*, 2009). Assuming steady-state conditions, O₂ fluxes from the mixed layer represent a balance between net biological production and sea-air exchange, allowing the calculation of NCP from sea-air flux estimates. Steady state assumptions are violated in upwelling systems, such as the CCS, where O₂ fluxes in the mixed layer are also affected by vertical mixing. However, such vertical mixing effects can be corrected using N₂O as a tracer



of O₂-depleted deep water, as oxygen-consuming N₂O production pathways are photo-inhibited at the surface, resulting in fixed subsurface N₂O to O₂ ratios in the ocean (Cassar, Nevison and Manizza, 2014).

80

The various measurement techniques described above yield PP estimates in a number of different ‘currencies’, i.e. carbon, oxygen and electrons, each with different integration time scales (seconds to weeks). In theory, combining PP quantification approaches can fill data gaps (e.g. cloud or ice interference with satellite data, or missing years in time series operations), and provide deeper understanding of ocean metabolism. In practice, incorporating alternative measurement approaches requires 85 understanding of conversion rates between the various PP currencies. Predicting these conversion factors is challenging, as they vary in response to environmental conditions and phytoplankton taxonomy and physiology (Halsey and Jones, 2015; Schuback *et al.*, 2017; Hughes, Varkey, *et al.*, 2018; Hughes *et al.*, 2021). For example, the ETR_{PSII} : GPP ratio often exceeds the theoretical stoichiometry of 4 (Halsey and Jones, 2015), implying that redox potential generated at PSII is used for functions 90 other than carbon fixation, such as nitrogen uptake or cyclic electron transport. Similarly, differences between ETR_{PSII} and NCP represent combined O₂ consumption pathways, including cellular respiration, chloro- and photorespiration and pseudo cyclic electron transport. Investigating the drivers of decoupling between currencies can thus improve conversion rate estimates, and also provide insights into energy transfer efficiencies between different components of the photosynthetic process.

95

Here we present simultaneous PP measurements in the CCS collected using high resolution, underway sampling techniques along a cruise track between Newport, OR and San Francisco, CA. Underway measurements of ETR_{PSII} and NCP were conducted during the May-June upwelling season of 2023 and were complemented with parallel measurements of ETR_{PSII} and ¹⁴C-GPP collected at oceanographic stations. Our results demonstrate fine-scale spatial patterns in GPP and NCP associated 100 with variability in localized upwelling filaments, with particularly notable differences observed across gradients of dissolved iron concentrations resulting from varying coastal bathymetry. These results enable us to examine variability in productivity currency conversion factors across natural Fe availability gradients within the California Current System, with potential application to other complex coastal waters.

2 Methods and Materials

2.1 Sampling Sites

105

Measurements were collected along the Oregon and Northern California coast during the Phytoplankton UPwelling Cycle (PUPCYCLE II) expedition, onboard the *R/V Sally Ride* from May 27 – June 11, 2023. A key objective of the program was to examine the evolution of phytoplankton blooms in recently upwelled waters, and we specifically targeted two upwelling plumes off Cape Blanco and Cape Mendocino, which were identified by low sea surface temperature (SST < 10°C; Figure 1). Along the cruise track, temperature, salinity, and chlorophyll fluorescence were monitored by the ship’s underway system, 110 supplied by a seawater supply line with a nominal intake depth of approximately 5m. Nitrate concentrations were measured continuously with a Seabird SUNA sensor. In addition to standard oceanographic variables, the seawater supply line was also used for continuous underway measurements of phytoplankton photo-physiology and ETR_{PSII} using a Fast Repetition Rate fluorometer (FRRF; Soliense Inc.), and NCP using a custom-built Pressure In-Situ Gas Instrument (PIGI), as described below.



115

120

125

130

135

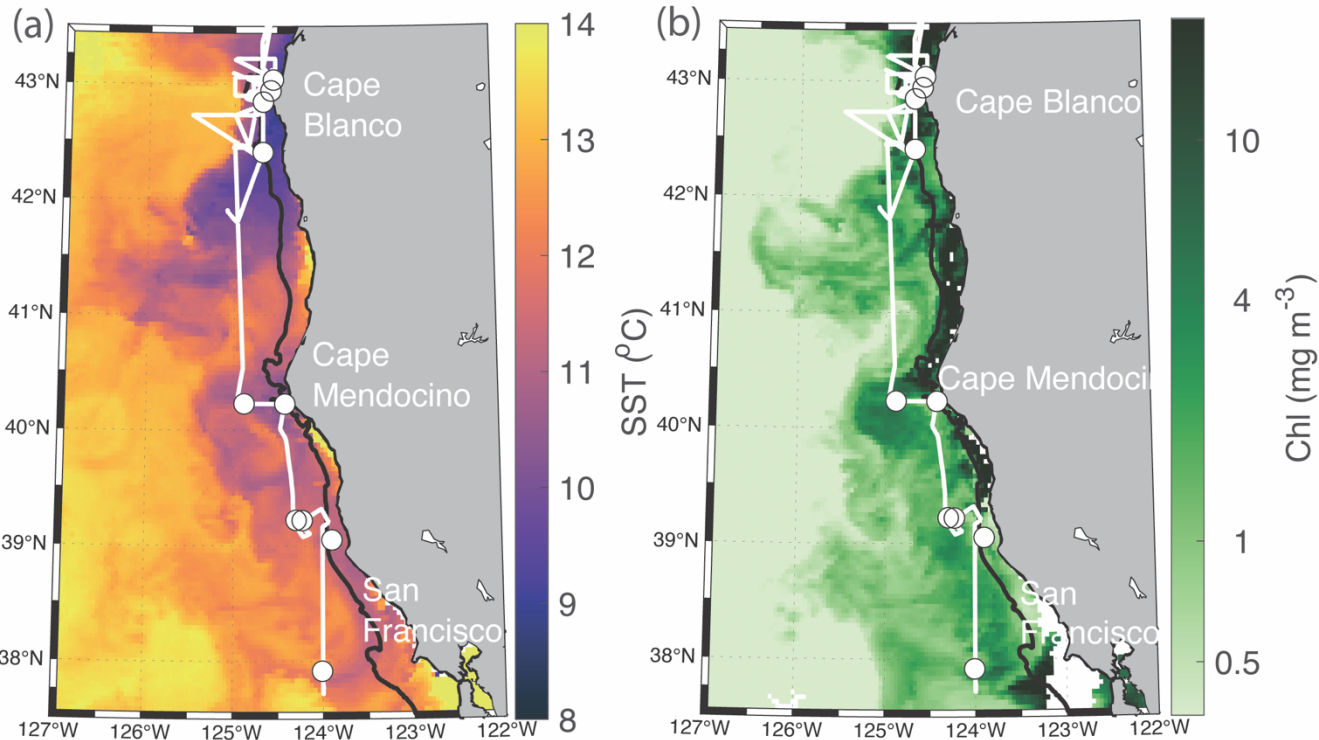


Figure 1. Study site map. Location of the cruise track (white line) and discrete sampling stations (white circles) during the PUPCYCLE expedition. The black bathymetric contour line represents the 200 m isobath. The study region and surrounding waters are colored by **a.** daily NASA Aqua Modis Level 3 satellite retrievals of Chl concentration (Chl) averaged over the cruise period (May 27 – June 11, 2024) **b.** NASA Aqua Modis Level 3 satellite retrievals of Sea Surface Temperature (SST) averaged over the cruise period.

Daily CTD and rosette casts were conducted one hour before local sunrise, and samples were collected at four depths targeting 1%, 10%, 22%, and 46% of surface solar irradiance levels. Photosynthesis-Irradiance (PI) curves (measured with Fast Repetition Rate fluorometry – see below), chlorophyll *a* (Chl) and nutrient concentrations (NO_3^- , Si, PO_4^{3-} , Fe) were measured at all four depths. Samples collected from 1% and 46% irradiance levels were also incubated for ^{14}C -based PI curves (see sect. 2.5), with sub-samples collected for High Performance Liquid Chromatography (HPLC)-based analysis of phytoplankton pigments.

2.2 Fast Repetition Rate Fluorometry

A bench-top Soliense Inc. Fast Repetition Rate Fluorometer (FRRF) was configured for underway collection of chlorophyll *a* fluorescence transients following Sezginer *et al.*, (2021). Samples were introduced to the measurement cuvette by an integrated peristaltic pump. The pump was used to flush the measurement cuvette for 2.5 minutes before isolating a sample for analysis. Following a one-minute dark period to relax short lived non-photochemical quenching, five single-turnover fluorescence transients were collected from each sample in the dark. Each single-turnover transient included a sequence of 100 sub-saturating excitation light pulses of $1.5\ \mu\text{s}$ duration, and a $1\ \mu\text{s}$ interval between pulses. The excitation phase is designed to stimulate photochemistry and gradually reduce the pool of primary electron acceptor molecules, Q_a (Kolber, Prášil and Falkowski, 1998). As the Q_a pool is reduced, further electron exchange between PSII and Q_a is prevented, closing the photochemistry pathway and causing a concurrent increase in PSII fluorescence yields. The excitation phase is followed by a relaxation sequence consisting of 127 light pulses with an initial $20\ \mu\text{s}$ interval. During the relaxation phase, the interval



140 between light pulses increases exponentially, enabling Q_a reoxidation between pulses to gradually reopen the photochemistry pathway, such that fluorescence yields return to their basal levels. The biophysical model described by Kolber, Prášil and Falkowski (1998) was fit to the resulting fluorescence transient to derive the maximum quantum yield of PSII (F_v/F_m), functional absorption area of PSII (σ_{PSII}), and turnover rate of the primary electron acceptor Q_a (τ_{Qa}).

2.3 Electron Transport Rates, ETR_{PSII}

145 Continuous FRRF sampling was interrupted every 12 samples (~3hrs) to conduct a Photosynthesis-Irradiance (PI) curve characterizing light-dependent changes in photo-physiology and photochemistry. Across the entire cruise, we collected 91 PI curves. Each PI curve was initiated with a fresh sample, and consisted of 11 light levels, increasing from 0 – 850 μmol photons $\text{m}^{-2} \text{s}^{-1}$. Light was supplied evenly by the five actinic LEDs within the FRRF (445, 470, 505, 530, and 590 nm). At each light level, ETR_{PSII} was calculated following Suggett and Moore (2010):

$$ETR_{PSII} = PAR * \sigma'_{PSII} * \frac{F'_q}{F'_v} * 6.033 * 10^{-3} \quad 1.$$

150

In this formulation, the rate of photon delivery to the pool of PSII reaction centers (RCII) is derived as the product of photosynthetically active radiation (PAR; units μmol photons $\text{m}^{-2} \text{s}^{-1}$) supplied by the LED lamps, and the wavelength-specific functional absorption area of RCII (σ'_{PSII} ; units of $\text{\AA}^2 \text{PSII}^{-1}$). The conversion efficiency from light to photochemical energy depends on the fraction of open RCII, measured as the dimensionless ratio between the fluorescence amplitude measured under actinic light when photochemistry is active ($F'_q = F'_m - F'$) and that measured under actinic light if all RCII were oxidized, ($F'_v = F'_m - F'_o$). In practice, measuring the minimum fluorescence when the RCII pool is completely open (F'_o) is challenging, as actinic light always drives some degree of photochemistry and reduction of RCII. Alternatively, F'_o can be derived as $F'_o/(F_v/F_m + F'_o/F'_m)$, following Oxborough *et al.* (2012).

160

The prime notation ('') refers to FRRF parameters derived under actinic light. The constant $6.033 * 10^{-3}$ converts PAR to units of quanta $\text{m}^{-2} \text{s}^{-1}$, and σ'_{PSII} to units of $\text{m}^2 \text{RCII}^{-1}$, so the final units of ETR_{PSII} are quanta $\text{s}^{-1} \text{RCII}^{-1}$. For a complete description of FRRF derived parameters, see Schuback *et al.* (2021) and (Tortell, Schuback and Suggett, 2023).

165

For each light curve measured, ETR_{PSII} was plotted against PAR and fit with the photosynthesis-irradiance model of Platt *et al.* (Platt, Gallegos and Harrison, 1980):

$$ETR_{PSII} = P_s \left(1 - e^{-\frac{\alpha PAR}{P_s}} \right) e^{-\frac{\beta PAR}{P_s}} \quad 2.$$

170

During the initial light-limiting part of the curve, ETR_{PSII} increases linearly with PAR with a slope of α . As PAR increases to saturating levels, ETR_{PSII} stabilizes at maximum levels, P_{max} . The light saturation index, E_k is derived as P_{max}/α . When phytoplankton are affected by photoinhibition, β describes the decrease in ETR_{PSII} at high light levels (i.e. $\gg E_k$). In the absence of photoinhibition, $P_s = P_{max}$. When photo-inhibition is present ($\beta > 0$), P_s represents the theoretical maximum potential ETR_{PSII} . When $\beta > 0$, P_{max} is derived as:

$$P_{max} = P_s \left(\frac{\alpha}{\alpha + \beta} \right) \left(\frac{\beta}{\alpha + \beta} \right)^{\frac{\beta}{\alpha}} \quad 3.$$

175

To evaluate ETR_{PSII} over the cruise track, we linearly interpolated derived values of α , β , and P_s to the sampling resolution of continuous PAR measurements from the ship's meteorological tower (Biospherical Inst. QSR-240P). In-situ mean mixed layer PAR was estimated by accounting for light attenuation with depth, quantified by the diffuse attenuation coefficient ($K_d = \ln(PAR_0/PAR_{mld})/(mld - 0)$), where PAR_0 is PAR measured at the surface and PAR_{mld} is PAR measured at the mixed layer



depth (mld) (Domingues and Barbosa, 2023). For each CTD cast ($n = 28$), mld was determined using a density difference criterion of 0.125 kg m^{-3} , and PAR_{mld} was measured with a Biospherical QSP-200 PAR sensor mounted to the CTD rosette. Both K_d and mld were linearly interpolated to the resolution of continuous PAR measurements. Finally, in-situ PAR was estimated as,

$$\text{PAR}_{\text{in situ}} = \text{PAR}(1 - e^{-K_d \text{MLD}})(K_d * \text{mld})^{-1} \quad 4.$$

To compare ETR_{PSII} with NCP (Sect. 2.6), we converted ETR_{PSII} from $e^- \text{RCII}^{-1} \text{ s}^{-1}$ to volumetric units of $\text{mmol O}_2 \text{ m}^{-2} \text{ d}^{-1}$. This conversion requires an estimate of the chlorophyll content of RCII, which is known to vary significantly across phytoplankton in response to taxonomic and environmental influences (Greene *et al.*, 1992; Murphy *et al.*, 2017; Aardema *et al.*, 2024). Following previous authors (Kolber and Falkowski, 1993; Schuback, Schallenberg, Duckham and Maldonado, 2015), we assumed a possible range of Chl to RCII ratios of 400 to 700, yielding upper and lower bounds of Chl-normalized ETR_{PSII} .

$$GP = \text{ETR}_{\text{PSII}} * 86400 * (\text{Chl:RCII})^{-1} * \text{Chl} * \text{mld} * \frac{1}{4} \quad 5.$$

To obtain volumetric units, Chl-normalized ETR was multiplied by mixed layer Chl concentrations ($\text{mmol Chl m}^{-3} * \text{mld}$), assuming homogenous [Chl] throughout the mixed layer. Multiplying by 86400 converts from s^{-1} to d^{-1} . Given that four charge separation events are required per O_2 evolved, ETR was divided by 4 for final gross photochemistry (GP) estimates in terms of $\text{mmol O}_2 \text{ m}^{-2} \text{ d}^{-1}$.

2.4 Non-Photochemical Quenching, NPQ

Under excess irradiance, light supply to PSII outpaces maximum downstream electron transport rates, creating the potential for dangerous reactive oxygen species (ROS) to accumulate (Müller, Li and Niyogi, 2001). To mitigate excess excitation, photoautotrophs have evolved a number of photoprotective mechanisms, including non-photochemical quenching (NPQ), which dissipates excitation absorbed by PSII as heat, thereby reducing PSII photochemical and fluorescence yields. Previously, NPQ has been quantified from FRRF data as Stern-Volmer quenching, defined as the relative decrease in PSII fluorescence in response to light exposure: $\text{NPQ}_{\text{SV}} = (F_m - F'_m)/F'_m$. However, this formulation does not account for longer-lived NPQ mechanisms that may still be active during dark measurements following recent high light exposure. To overcome this limitation, we used the normalized Stern-Volmer parameter (NPQ_{NSV}), calculated as F'_0/F'_v (McKew *et al.*, 2013). For each PI curve measured, NPQ_{NSV} was plotted against PAR and fit with a single component exponential curve. In-situ NPQ_{NSV} was then estimated by interpolating the resulting curve fits to in-situ PAR values.

2.5 ^{14}C -uptake experiments

During daily station sampling, 200 mL were collected from 1% and 46% light level depths (approximately 50 and 10 meters, respectively) into acid washed 250 mL bottles for ^{14}C incubations. Samples were immediately spiked with $150 \mu\text{Ci}$ of H^{14}CO_3 (Perkin Elmer), and inverted to homogenize the contents of the bottles. The homogenized media was then aliquoted into 20 mL borosilicate scintillation vials, which were incubated over 3 hours in a custom-built photosynthetron at 7 light levels from $0 - 650 \mu\text{mol photons m}^{-2} \text{ s}^{-1}$. At the end of the incubation, the entire content of the vials was filtered onto 25mm GF/F filters with a nominal pore size of $0.7 \mu\text{m}$. Filters were fumed with 10% HCl for 24 hours to remove any inorganic carbon prior measuring activity on filters with an on-board scintillation counter (Beckman LS 6500). Immediately after spiking samples, three vials were filtered for triplicate time zero measurements. Three 100 μL aliquots were also taken from the initial 200 mL sample and treated with 100 μL of 3M NaOH to measure total ^{14}C counts. Disintegrations per minute were converted into hourly C fixation rates according to Knap *et al.*, (1996).



2.6 Net Community Productivity (NCP)

We measured NCP based on mixed layer concentrations of O₂ and N₂ obtained from the Pressure of In-Situ Gas Instrument (PIGI), following Izett and Tortell, 2021 and Izett *et al.*, 2021. This method estimates NCP from the biological oxygen saturation anomaly, ΔO₂/N₂', using N₂' as an analog for Argon (Ar) to correct for physical effects on O₂ saturation. In this method, net community productivity is equated to the sea-air flux of O₂ as determined by the biological saturation anomaly (ΔO₂/N₂') scaled by the [O₂] in equilibrium with the atmosphere ([O₂]_{sat}), and the O₂ piston velocity (k_{O_2}).

$$NCP = k_{O_2} * \frac{\Delta O_2}{N_2'} * [O_2]_{sat} \quad 6.$$

The PIGI enables cost effective measurements of ΔO₂/N₂' using an oxygen optode and a gas tension device rather than a mass spectrometer, which is more commonly used to measure ΔO₂/Ar (Izett and Tortell, 2020). In this method, N₂' is derived as an approximation of Ar, using model calculations that quantify differences between Ar and N₂ concentrations due primarily to solubility changes and bubble processes. A full description of the 1D model applied to estimate N₂' is available in Izett and Tortell (2021). The model uses ancillary data, including windspeed, mixed layer depth, temperature, salinity, and sea level pressure, to estimate changes in mixed layer Ar and N₂ concentrations over one residence time period prior to sampling. We applied a residence time of 14 days for this region where mixed layer gas residence times are strongly influenced by the timescales of upwelling events (Austin and Barth, 2002). Ancillary datasets required for N₂' calculations were obtained from a combination of satellite observations and model products, and are compiled in the Supplement S1, alongside descriptions of each data source. The 1D model calculations and code are available at https://github.com/rizett/O2N2_NCP_toolbox with example calculations.

Additional corrections to NCP estimates were made to account for vertical mixing fluxes, which transport low O₂ water to the surface (Izett *et al.*, 2018). Previous studies have omitted ΔO₂/Ar data collected in known upwelling areas, where the assumption of limited vertical mixing fluxes on ΔO₂/Ar variability is violated (e.g. Stanley *et al.*, 2010). To address this limitation, Cassar, Nevison and Manizza (2014) developed an approach to use surface measurements of N₂O to quantify vertical transport of low O₂ waters. In marine environments, there is a strong stoichiometric relationship between apparent oxygen utilization and N₂O, which is produced as a by-product of subsurface oxygen-consuming N remineralization pathways (Elkins *et al.*, 1978). These N₂O production pathways are thought to be photo-inhibited within the euphotic zone (Horrigan, Carlucci and Williams, 1981; Olson, 1981), so that excess N₂O concentrations in the mixed layer serve as a tracer for vertical influxes of O₂-depleted subsurface water. We note that several recent studies have observed nitrification within the euphotic zone, challenging the assumption that N₂O production is limited to subsurface waters (Grundle, Juniper and Giesbrecht, 2013; Smith *et al.*, 2014). However, a sensitivity analysis by Izett *et al.* (2018) determined the potential effects of euphotic zone nitrification introduced a nearly negligible error to NCP estimates in regions with high productivity and high mixing rates, as is the case in the CCS. We thus used the approach of Cassar, Nevison and Manizza (2014) and Izett *et al.*, (2018), to correct for vertical mixing following Eq. 7.

$$NCP = k_{O_2} * \left(\frac{\Delta O_2}{Ar} * [O_2]_{sat} - \frac{k_{N_2O}}{k_{O_2}} * \frac{\partial [O_2]^B}{\partial [N_2O]^B} * [N_2O]^B \right) \quad 7.$$

This mixing correction uses surface measurements of N₂O super-saturation ([N₂O]^B), the 'supply ratio' of oxygen saturation, given by the vertical gradient of biological O₂ to N₂O ($\frac{\partial [O_2]^B}{\partial [N_2O]^B}$), and the ratio of gas transfer velocities ($\frac{k_{N_2O}}{k_{O_2}}$). The surface water saturation of N₂O, [N₂O]^B, was derived based on the difference between the N₂O saturation anomaly and changes in N₂O solubility due to recent heat fluxes ([N₂O]_{meas} - [N₂O]_{sat} - [N₂O]_{thermal}). Heat flux effects on solubility, [N₂O]_{thermal}, were derived following Keeling and Shertz (1992), with corrections from Jin *et al.* (2017). Surface [N₂O]_{meas} was continuously measured from the surface seawater supply with an integrated cavity output spectroscopy (OA-ICOS) gas analyzer (Los Gatos Research, N₂O/CH₄ Analyzer, Model Number: 913-0055) coupled to a gas extraction module (Schuler and Tortell, 2023). The region-specific supply ratio, $\frac{\partial [O_2]^B}{\partial [N_2O]^B}$, was calculated by taking the slope of subsurface [O₂]^B plotted against subsurface [N₂O]^B.



260 The compiled data across the cruise track resulted in a supply ratio of $-1.6 * 10^4 \pm 0.3 * 10^4$ mmol O₂ (mmol N₂O)⁻¹, which is similar to previous measurements for the Northeast Pacific ($-1.8 * 10^4$; Izett et al., 2018) and global basins ($-1.5 * 10^4$;(Cassar, Nevison and Manizza, 2014). Following Cassar, Nevison and Manizza (2014), we assumed a constant $\frac{K_{N_2O}}{K_{O_2}}$ ratio of 0.92. Total uncertainty was determined by following Izett (2021).

2.7 Nutrient concentrations

265 Samples collected during daily productivity casts were analysed for dissolved NO₃⁻ + NO₂⁻, PO₄³⁻, and silicic acid concentrations. Thirty mL were collected from niskin bottles and filtered onto GF/F filters, using acid-washed syringes into 20mL HDPE scintillation vials. Samples were kept frozen before analysis on a OI Analytical Flow Solutions IV auto analyzer by Wetland Biogeochemistry Analytical Services at Louisiana State University. Detection limits were 0.09 $\mu\text{mol L}^{-1}$ for nitrate + nitrate, 0.02 $\mu\text{mol L}^{-1}$ for phosphate and 0.02 $\mu\text{mol L}^{-1}$ for silicic acid. Reference standards for dissolved nutrients in seawater 270 were used to ensure quality control.

275 Samples for iron analysis were collected with a rosette of Teflon-coated OTE-bottles during a separate cast directly after the daily sampling cast. After recovery, OTE-bottles were taken directly to a trace metal-clean sampling van where they were pressurized with filtered compressed air. Surface samples (~3 m depth) were also collected with a tow-fish system plumbed into the trace metal van, as in Bruland et al. (2005). All samples were passed through pre-cleaned 0.2 micrometer Supor 280 membrane Acropak capsule filters into trace metal cleaned bottles (Cutter et al., 2014). Samples were acidified to pH 1.8 with optima HCl, and analyzed post-cruise with a flow injection analysis method (Lohan, Aguilar-Islas and Bruland, 2006), with modifications as in Biller et al. (2013). Briefly, this method involved pre-concentrating the Fe at pH 2 with Toyopearl Chelate-650 resin and eluting into a reaction stream containing the colorimetric agent N,N-dimethyl-p-phenylenediaminedihydrochloride (DPD). The absorbance of the reaction stream was measured with a flow-through spectrophotometer. Calibration was performed with a standard addition curve, and blanks were assessed using acidified MilliQ. Reference samples analysed to assess accuracy compared well to consensus values: SAFe D1 0.70 +/- 0.04 nmol Fe/kg, n=12 compared with consensus value 0.67 +/- 0.04 nmol/kg, and GEOTRACES GSC 1.51 +/- 0.07 nmol/kg (n=11) compared with consensus value 1.53 +/- 0.11 nmol/kg.

285 2.8 Transcriptomic analysis

290 Surface niskins (46% surface irradiance) collected during daily productivity casts were subsampled for RNA extraction. Approximately 2.5L to 4L of seawater were filtered onto 0.8 μm Pall Supor filters (142 mm) using a peristaltic pump, and then flash frozen in liquid nitrogen and stored at -80 °C. RNA was extracted using the RNAqueous-4PCR kit, following manufacturer instructions with the incorporation of a bead beating step during RNA lysis. All RNA samples were sent to GENEWIZ for library preparation and sequencing with PolyA tail selection. Sequencing was performed on an Illumina HiSeq 4000 with a 2x150 bp configuration. GENEWIZ provided raw paired-end read sequences for each sample.

295 Raw reads were trimmed using Trim Galore 0.6.10 (Martin, 2011) and quality control was determined with FastQC (Andrews, 2010). A *de novo* metatranscriptome assembly was conducted using rnaSPAdes 3.15.5 (Bushmanova et al., 2019) and CD-HIT-EST (Li and Godzik, 2006). Contigs were annotated using the Marine Functional Eukaryotic Reference Taxa (MarFERReT) database (Groussman et al., 2023), which provides NCBI taxonomic annotations (Federhen, 2012) and Pfam 34.0 functional annotations (Mistry et al., 2021). Samples were mapped against the MarFERReT DIAMOND sequencing aligner and its compatible BLASTX command (e-value < 1e-06) (Buchfink, Xie and Huson, 2015). Trimmed samples were aligned using Salmon (Patro et al., 2017). The package tximport (Soneson, Love and Robinson, 2016) was used to generate a comprehensive table of read count data for each sample and each contig. Only counts taxonomically mapping to 300 Bacillariophyta (i.e., diatoms) were included. The normalized counts for all genes were then calculated using DESeq2's median of ratios method (Love, Huber and Anders, 2014). Normalized counts of the low iron-inducible periplasmic protein (Fea1)



(Allen *et al.*, 2007), which shows high similarities to Iron Starvation-Induced Protein 2A (ISIP2A) (Behnke and LaRoche, 2020), was used as an indicator for iron stress (Marchetti *et al.*, 2017).

2.7 Pigment Concentrations and Taxonomic Compositions

305 During daily productivity casts, duplicate 1L dark Nalgene bottles were filled with water from niskin bottles collected at 1% and 46% PAR level depths. Under low ambient light, samples were filtered onto 47mm GFF filters (Whatman, nominal pore size $0.7 \mu\text{m}$). Filters were immediately flash frozen and stored in an onboard -80°C freezer. Samples were shipped on dry ice to the Pinckney Estuarine Ecology Photopigment Analysis Facility at the University of Southern California. There, 310 photopigment concentrations were determined with high performance liquid chromatography following (Pinckney *et al.*, 2001). Pigment compositions are reported in Appendix 2.

In addition to pigment sampling, Light microscopy was used to identify and enumerate dominant phytoplankton taxa. For 315 microscopic cell counts, 25-50 mL subsamples preserved in Lugol's solution were concentrated by sedimentation using Utermöhl chambers for >24h (Lund, Kipling and Le Cren, 1958). Cell counts of recognizable dinoflagellate and diatom genera were carried out using an Olympus CKX-31 inverted microscope in at least ten fields of view per sample at 200x and 400x magnification.

3 Results

3.1 Oceanographic conditions

320 Across the cruise track, sea surface temperature (SST) ranged from 8.5 to 14 °C (Fig. 2), with strong coastal to offshore gradients (Fig. 1 and 2). The lowest SST were observed within near-shore upwelling plumes, which were associated with high 325 salinity ($> 33 \text{ psu}$). Along the entire cruise transect, salinity was negatively correlated with SST ($\rho = -0.73$, $p << 0.01$), as expected for upwelling regions. Sharp hydrographic fronts were apparent along coastal to offshore transects. Moving offshore, SST rapidly increased, while salinity dropped, changing by as much as 2 degrees and 0.5 psu, respectively, within a span of 5 km. These results indicate the presence localized on-shore upwelling plumes, as compared to more homogenous off-shore 330 waters. Within the upwelling plumes, NO_3^- concentrations were elevated, reaching maximum concentrations of $20.5 \mu\text{M}$ and displaying a positive relationship with salinity ($\rho = 0.89$, $p << 0.01$) and a negative relationship with SST ($\rho = -0.76$, $p << 0.01$). Off-shore, NO_3^- decreased to concentrations below the SUNA detection limit ($\sim 0.3 \mu\text{M}$), highlighting the difference in nutrient availability between the oligotrophic offshore waters and productive coastal upwelling environments. Chlorophyll concentrations varied between 0.04 to 5.6 mg m^{-3} and exhibited a statistically significant (though weak) positive relationship with NO_3^- ($\rho = 0.30$, $p << 0.01$).

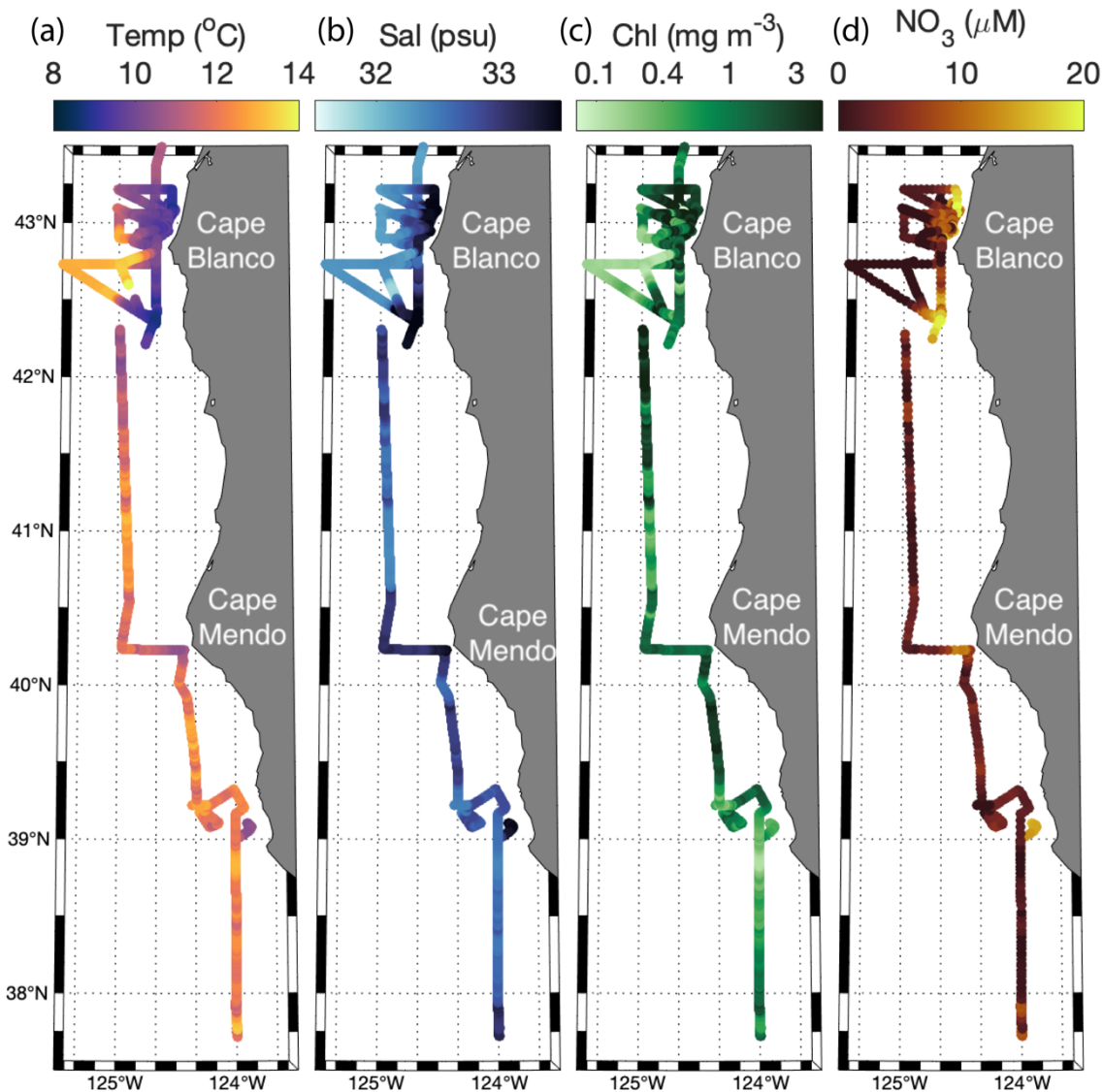


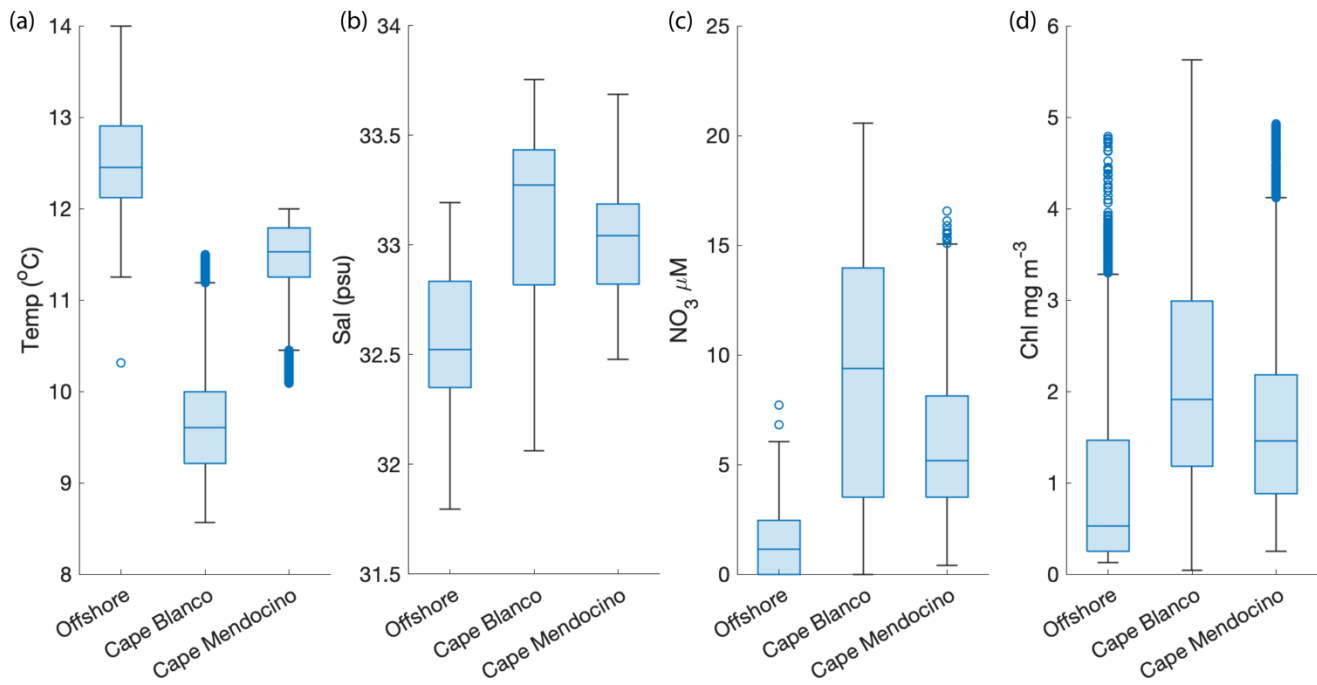
Figure 2. Surface water (a) SST, (b) salinity, (c) Chl, and (d) NO_3^- along the cruise track. Cape Mendocino is abbreviated as Cape Mendo.

335

In addition to the coastal-offshore gradient, surface water hydrography also differed between the two distinct upwelling plumes we sampled. These plumes were identified as low SST in the lees of Cape Blanco and Cape Mendocino (Fig 1). Both plumes exhibited an upwelling signature, but the apparent intensity of upwelling (as reflected in SST, salinity, NO_3^- , and Chl) was significantly stronger within the northern Cape Blanco plume (Fig. 3). Most apparently, SST was several degrees cooler at 340 Cape Blanco (median of $9.6 \pm 0.4^\circ\text{C}$) than at Cape Mendocino (median of $11.5 \pm 0.01^\circ\text{C}$). Nitrate concentrations were highly variable across both plumes, but the mean NO_3^- at Cape Blanco ($9.4 \pm 0.8 \mu\text{M}$) was nearly twice as high as that of Cape Mendocino ($5.2 \pm 0.4 \mu\text{M}$). Chlorophyll concentrations were elevated at both plumes relative to offshore waters, with a median of $1.9 \pm 0.01 \text{ mg m}^{-3}$ around Cape Blanco and $1.4 \pm 0.01 \text{ mg m}^{-3}$ at Cape Mendocino. Both these Chl concentrations



345 are well below that which can be supported by the available NO_3^- concentrations ($1 \mu\text{M} \text{NO}_3^-$ can typically yield $1 \mu\text{g chl L}^{-1}$), indicating that the phytoplankton blooms were likely in the early phases of development following upwelling.



350 **Figure 3. Variability in SST (a), salinity (b), NO_3^- (c), and Chl (d) within the observed water masses offshore, at Cape Blanco, and Cape Mendocino.** The line inside each boxplot represents the median, while whiskers display the 75th percentile. Points outside the whiskers represent outliers.

Underway surface measurements were accompanied by on-station discrete sampling for NO_3^- , PO_4 , Si , and Fe concentrations. As expected, NO_3^- was highly correlated with PO_4 ($\rho = 0.99$, $p < 0.01$) and SiO_2 ($\rho = 0.92$, $p < 0.01$). The ratio of $\text{NO}_3^-:\text{PO}_4$ was 7.4 ± 2.0 , and less than half the expected Redfield ratio of 16. This result is consistent with observations of low $\text{NO}_3^-:\text{PO}_4$ (~2-3) in the North Pacific attributed to high subsurface denitrification rates (Tyrrell and Law, 1997). In contrast with the strong covariance observed among macronutrients, surface Fe distributions were not correlated with surface NO_3^- concentrations ($\rho = 0.35$, $p = 0.6$). At Cape Blanco, Fe concentrations varied from 1.2 – 2.0 nM, whereas Cape Mendocino concentrations were significantly lower, ranging from 0.21 – 0.65 nM. Offshore Fe concentrations were relatively high, with a surface concentration of 0.29-0.42 nM. These waters exhibited low macronutrient concentration. In section 4.1 we explore the potential causes for different nutrient signatures in the various water masses we sampled.

3.2 Photo-physiology

365 Along the cruise track, phytoplankton photophysiological properties displayed spatial variability associated with hydrographic gradients, superimposed on significant diel cycles. In particular, we observed strong diel signatures in the expression of various photo-protective mechanisms. We observed decreases in the PSII functional absorption area, σ_{PSII} , throughout the day, followed by recovery overnight (Fig. 4a). The maximum photochemical efficiency of PSII (F_v/F_M) similarly decreased during the day and peaked overnight. Measurements of NPQ_{NSV} displayed an inverse diel pattern to those of σ_{PSII} and F_v/F_M ,



reflecting adjustments to the allocation of absorbed energy between competitive photochemistry and thermal dissipation pathways. These observations agree with previous diel cycle studies of the region (Schuback and Tortell, 2019).

370

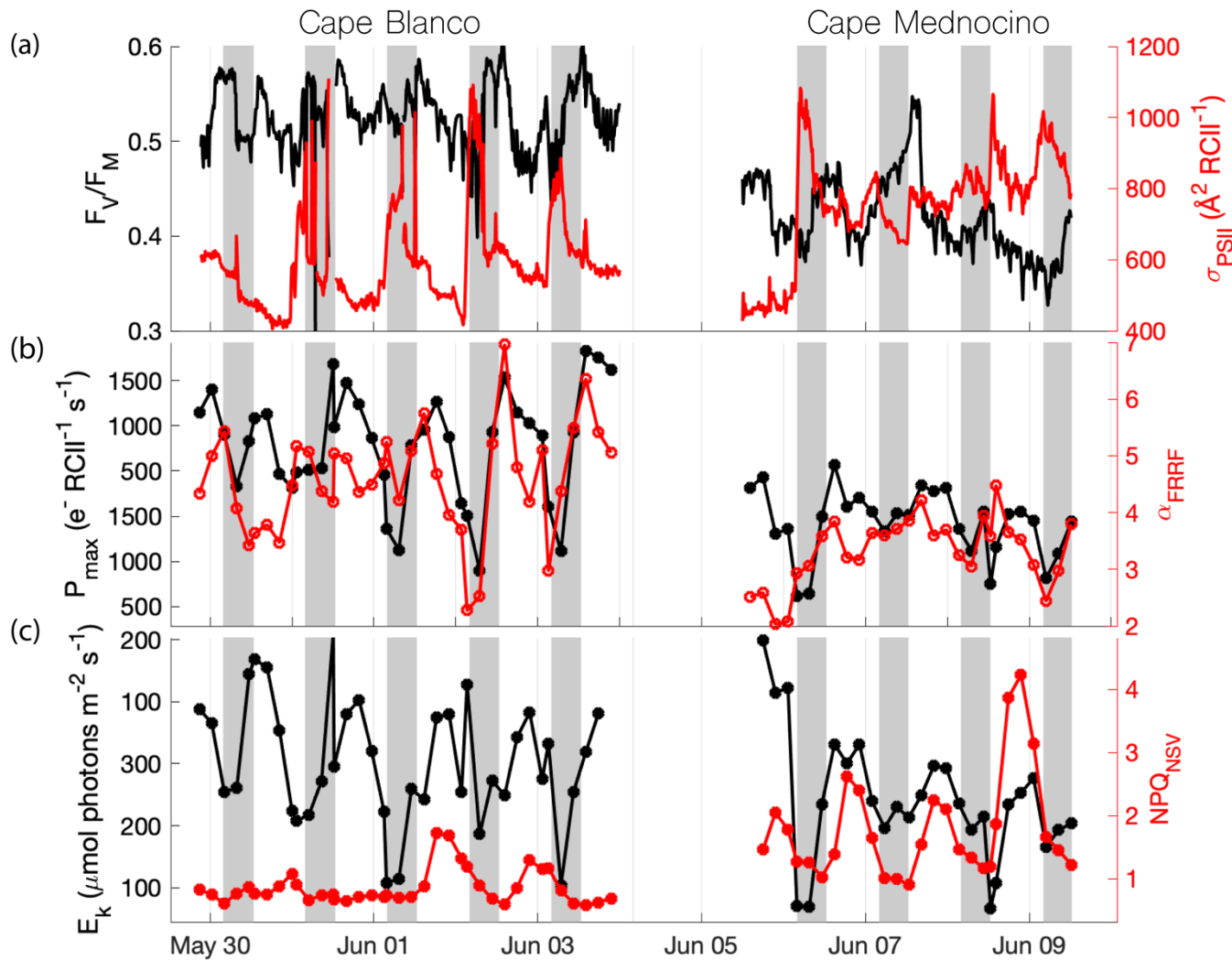


Figure 4. Diel patterns in photo-physiological properties along the cruise track. Grey shading indicates night-time, when surface PAR $< 5 \mu\text{mol photons m}^{-2} \text{s}^{-1}$. **a.** F_v/F_M (black) and σ_{PSII} (red), **b.** P_{\max} (black) and α (red), **c.** E_k (black) and NPQ_{NSV} (red) are displayed with respect to sampling time. High sea states between 06/04 – 06/06 impacted the seawater intake, resulting in the data gap.

375

Photosynthetic parameters derived from semi-continuous PI curves also exhibited diel patterns that mirrored those of F_v/F_M and σ_{PSII} . The maximum, light-saturated, ETR_{PSII} (P_{\max}) and the light utilization efficiency under light limiting conditions (α) both peaked during the midday when *in-situ* irradiance was highest. The light saturation level, E_k , tracked surface light availability, while the photoinhibition parameter (β) peaked during midday and diminished overnight. As with the continuous underway data, results from these discrete PI curves match the previous diel observations of Schuback and Tortell (2019). We note, however, that there is potential for some convolution of temporal and spatial variability, as the ship spent more time

380

offshore in the night, and on-shore during the daytime. It is thus possible, that some of the diel cycling partially reflects different photo-physiological signals between coastal and offshore waters.

385

Beyond diel signals, we also observed significant gradients in photophysiological parameters in relation to oceanographic conditions. Elevated values of Fv/F_M , P_{max} , and α were observed in regions of localized upwelling (Table 1), indicating that the vertical transport of nutrient-rich water to the surface supported high photochemical yields. In contrast, signs of upwelling were associated with decreased σ_{PSII} and NPQ_{NSV} . Notably, the two upwelling plumes (near Cape Blanco and Cape 390 Mendocino) showed significantly different phytoplankton photophysiological properties. At Cape Blanco, mean values of NPQ_{NSV} and σ_{PSII} were significantly lower than at Cape Mendocino, while Fv/F_M , P_{max} , α , and β were all higher at this site, compared to Cape Mendocino (Table 1). Photophysiological properties at Cape Mendocino were much closer to those observed in offshore non-upwelling waters, with mean Fv/F_M values that were lower than offshore, despite elevated macro-nutrient concentrations. This result, combined with low Fe concentrations at Cape Mendocino, suggests that phytoplankton at Cape 395 Mendocino were Fe-stressed despite the presence of upwelling conditions (see Discussion).

	CAPE BLANCO	CAPE MENDOCINO	OFF- SHORE	SST N= 71604	SAL N= 71604	NO ₃ ⁻ N= 989	FE N= 40	SI N= 40	PAR N= 71604
Fv/F_M N= 1438	0.47±0.01 ^A	0.39 ± 0.08 ^B	0.41± 0.08 ^C	-0.55*	0.27*	0.39*	0.32	0.52	-0.04
σ_{PSII} , N= 1438	545 ± 5 ^A	655 ± 11 ^B	647 ± 5 ^C	0.58*	-0.38*	-0.45*	-0.55	-0.60	-0.12
P_{max} , N = 91	977±83 ^A	600 ± 42 ^B	600 ± 91 ^B	-0.67*	0.40*	0.50*	0.45	0.78*	0.19
α , N = 91	4.8±0.3 ^A	3.3 ± 0.3 ^B	3.6 ± 0.4 ^B	-0.57*	0.19	0.24	0.37	0.45	-0.11
E_k , N = 91	210±19 ^A	172 ± 20 ^B	176 ± 15 ^B	-0.38*	0.33*	0.41*	0.62	0.72*	0.37*
NPQ_{NSV} , N = 91	0.75±0.05 ^A	1.33 ± 0.2 ^B	1.2 ± 0.2 ^B	0.66*	-0.26	-0.46	-0.36	-0.62	0.58*

400 **Table 1. Summary of photophysiological properties at each sampling environment and their relationship to hydrographic parameters.** Left side of the table displays the median ± median absolute deviation for each photophysiological parameter according to sampling environment. Superscripts denote groups with significantly different medians. Right side of the table displays spearman rank correlation coefficients for each photophysiological parameter against environmental parameters. * indicates $p < 0.05$. Due to differences in sampling frequencies, the number of observations (N) varied across different parameters. For correlation analyses, paired observations were matched in space and time to the lowest resolution measurement.

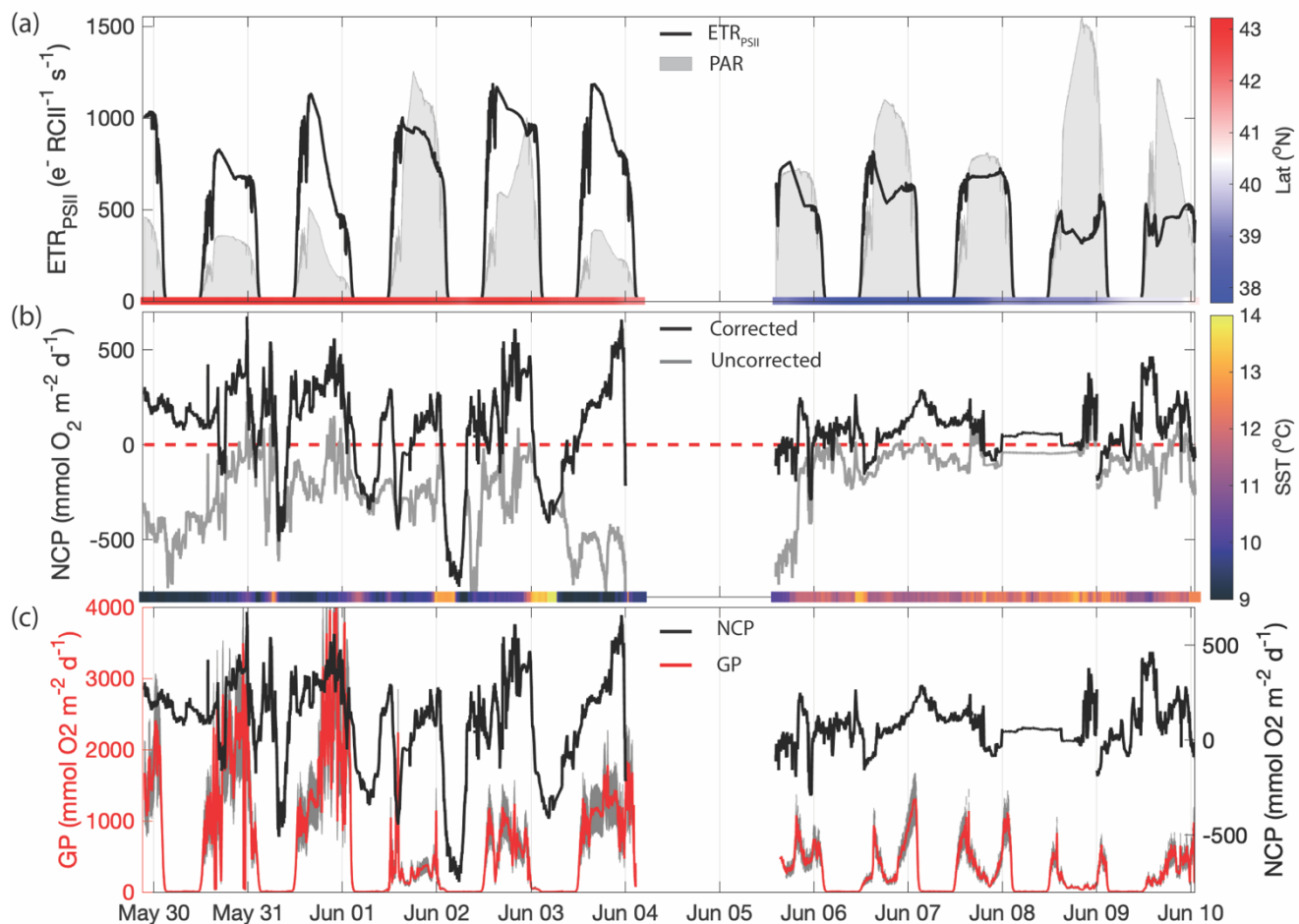
405 3.3 Primary Productivity

3.3.1 Electron Transport Rates, ETR_{PSII}

In-situ ETR_{PSII}, followed a notable diel cycle due to its first order dependency on irradiance (Eq 1, Fig. 5a). However, the relationship between PAR and ETR_{PSII} was spatially variable across the cruise track, reflecting differences in α_{FRRF} , P_{max} , and E_k between Cape Blanco and Cape Mendocino (Table 1; Fig. 4). The amplitude of diel ETR_{PSII} was greatest near Cape Blanco, 410 despite lower average mixed layer PAR (Fig 4a). At Cape Blanco, maximum ETR averaged 977±83 e⁻ RCII⁻¹ s⁻¹, as compared



to maximum values of only $600 \pm 42 \text{ e}^- \text{RCII}^{-1} \text{ s}^{-1}$ at Cape Mendocino. The higher maximum ETR at Cape Blanco is in good agreement with the observations of higher photochemical yields in this region (Table 1).



415 **Figure 5. Primary productivity time series along the cruise track.** **a)** ETR_{PSII} derived from FRRF-measured PI curve parameter interpolated to match NCP sampling frequency (black line). The grey patches indicate the mean PAR available within the mixed layer. The bar on the bottom is coloured by the sampling latitude. The Cape Blanco filament is designated as latitude > 40.5 and is coloured red, while Cape Mendocino is designated as latitude < 40.5 coloured blue. **b)** Uncorrected NCP (grey) and mixing-corrected NCP (black). The dashed red line denotes the boundary between net autotrophy (NCP > 0) and net heterotrophy (NCP < 0). The color bar on the bottom illustrates the sample temperature. **c)** mixing-corrected NCP (black, right y-axis) and gross photochemistry (GP), shown in red (left y-axis). GP is calculated by converting ETR_{PSII} from units $\text{e}^- \text{RCII}^{-1} \text{ s}^{-1}$ to $\text{mmol O}_2 \text{ m}^{-2} \text{ d}^{-1}$. The grey shading around the red line displays the range of GP based on an assumed range of 400 – 700 Chl:RCII.

3.3.2 Net Community Productivity, NCP

425 In addition to GPP, we estimated NCP from underway measurements. Prior to correcting for vertical mixing, more than 80% of derived NCP values were less than 0, suggesting net heterotrophic conditions over most of the cruise track. The most



negative uncorrected NCP values were observed near Cape Blanco, despite the high gross photochemistry rates measured in this region.

430 The apparent decoupling between NCP and GPP can be largely explained by vertical mixing of low O₂ waters, which artificially depress O₂-derived NCP estimates (see Sect. 2.4). After applying the N₂O-based mixing correction, we found that the majority of the cruise track (73% of measurements) exhibited net autotrophy, with the highest value recorded within the Cape Blanco filament. For the most part, net heterotrophy only existed at night in warmer off-shelf waters. The mean corrected NCP was 80 ± 218 mmol O₂ m⁻² d⁻¹, within range of previous observations of late-spring NCP within the California Current (Kranz *et al.*, 2020). The large standard deviation reflects the large diel and spatial variability observed along the cruise track. 435 The highest NCP estimates we obtained (> 500 mmol O₂ m⁻² d⁻¹) are on the upper end of previous measurements. Values above 100 mmol O₂ m⁻² d⁻¹ have only been observed in the most productive coastal waters (Wang *et al.*, 2020; Niebergall *et al.*, 2023), further emphasizing the high productivity of the CCS.

440 The N₂O-derived mixing correction term was strongly correlated to N₂O-independent indicators of upwelling, namely temperature ($\rho = -0.77$, $p < 0.01$). These results give confidence that high surface concentrations of N₂O are a valid marker of upwelling and transport of O₂-poor subsurface water into the mixed layer. The maximum correction factor, 1200 mmol O₂ m⁻² d⁻¹, was observed within the cold upwelling filament near Cape Blanco, where uncorrected NCP was below -500 mmol O₂ m⁻² d⁻¹. This result highlights the impact of vertical fluxes on O₂-based NCP estimates in upwelling regions.

445 3.3.3 Carbon fixation rates

At nine discrete sampling stations, ¹⁴C-based PI curves were measured in parallel with ETR_{PSII} at the surface and at the base 450 of the euphotic zone. Volumetric carbon fixation rates varied significantly between stations and depths. Maximum carbon fixation rates (carbon-based F_{max}) ranged from 0.4 to 96 $\mu\text{g C L}^{-1} \text{ hr}^{-1}$. Over 85% of the variability in carbon fixation rates could be explained by differences in biomass, which varied from 0.11 to 9 mg Chl L⁻¹. Chlorophyll concentrations in near-surface waters were, on average, four times higher than those at the base of the euphotic zone, implying the bulk of carbon fixation took place in the mixed layer. The bottom depth of the euphotic zone was $x \pm y$ times greater, on average, than the bottom depth of the mixed layer.

455 To compare carbon-based GPP estimates against parallel ETR_{PSII} measurements, carbon fixation rates were normalized to chlorophyll and converted to units of C chl⁻¹ s⁻¹. Chlorophyll normalized carbon fixation rates were positively correlated with Fe ($\rho = 0.40$, $p < .05$), Fv/FM ($\rho = 0.56$, $p < .05$), and Si:NO₃⁻ ratios ($\rho = 0.60$, $p < .05$), and negatively correlated with σ_{PSII} ($\rho = -0.68$, $p < .05$). These results suggest that stations with low chlorophyll-normalized carbon fixation rates may have been affected by Fe and Si co-limitation. By comparison, carbon fixation rates were not significantly correlated with NO₃⁻ or PO₄ concentrations or salinity.

460 Notably, carbon fixation consistently saturated at lower light intensities than ETR_{PSII}. The average E_k for ETR_{PSII} was 5 ± 2.8 times greater than E_k for carbon fixation. As a result, carbon fixation did not scale linearly with ETR_{PSII}, but rather demonstrated a hyperbolic relationship at each station and depth sampled. At sub-saturating light levels, carbon fixation increased linearly with ETR_{PSII}, until approaching an asymptote as ETR_{PSII} continued to increase while carbon-fixation remained stationary (Fig 465 6). This result indicates that at light levels beyond the saturating index for carbon-fixation, ETR_{PSII} provides reducing power in excess Calvin-Benson Cycle requirements. Previous studies have noted a similar nonlinear relationship between carbon fixation and ETR_{PSII}, consistent with an upregulation of alternative electron pathways under high light levels (Suorsa, 2015; Zhu *et al.*, 2017; Schuback and Tortell, 2019). This non-linear relationship between C fixation and ETR has been cited as a key limitation to the widespread use of FRRF for autonomous high resolution GPP estimates. Although our results demonstrate 470 a clear hyperbolic relationship between these rates, the parameters describing this relationship were variable across stations. In sect. 4.3, we further examine the relationship between carbon fixation and ETR_{PSII}, and contextualize the apparent differences in carbon-electron decoupling with available physiological, and environmental data.

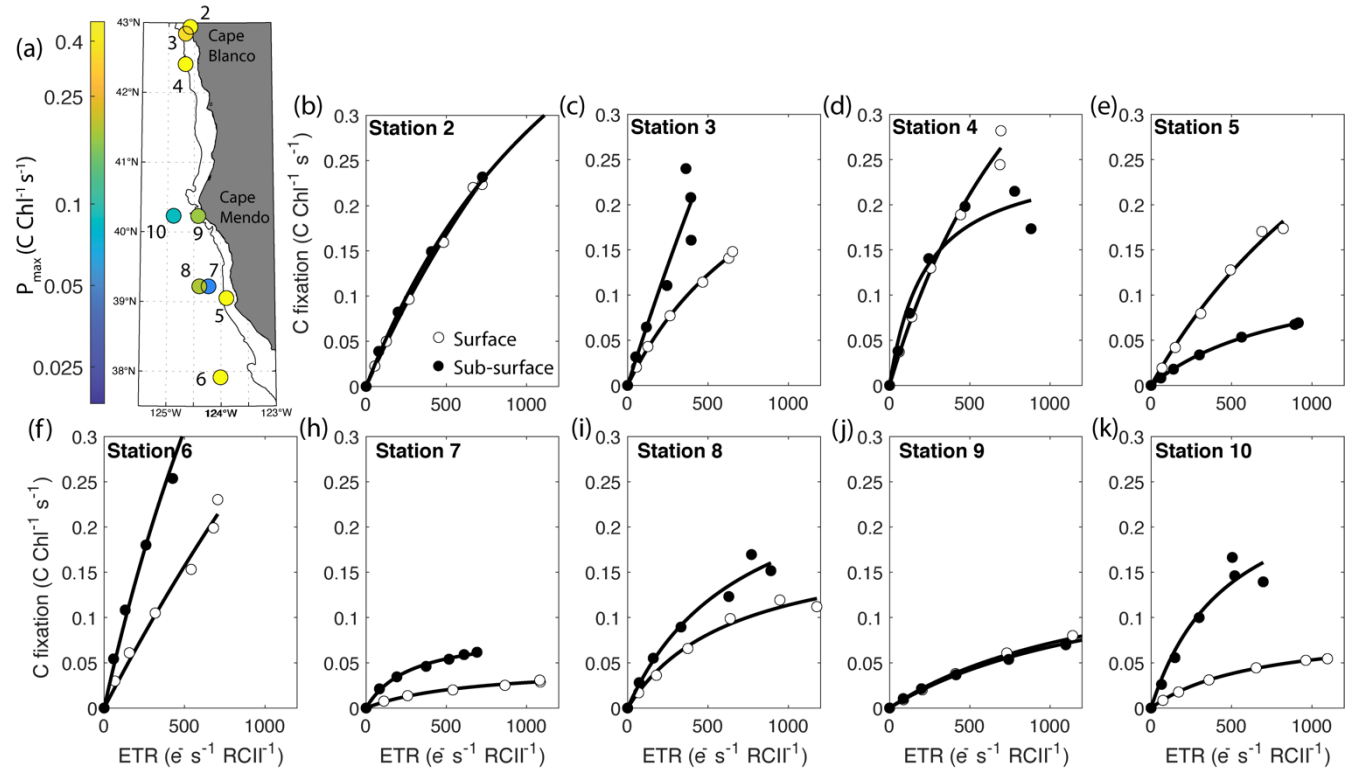


Figure 6. Parallel measurements of fluorescence- and ^{14}C -based photosynthesis-irradiance experiments conducted on-station. The top left displays the sample locations coloured by maximum chl-specific surface carbon fixation rates. The black contour line displays the 200m isobath. The other panels show carbon fixation rates plotted against ETR_{PSII} . Surface samples are represented by open circles while sub-surface samples are depicted as closed circles. Each curve is fit with the function,
$$C \text{ fixation} = \frac{C_{\text{max}} * \text{ETR}_{\text{PSII}}}{K_{\text{sat}} + \text{ETR}_{\text{PSII}}}$$
, where C_{max} is the maximum carbon fixation rate, and K_{sat} is the saturation constant beyond which changes in carbon fixation with respect to ETR_{PSII} become increasingly non-linear. Carbon fixation data were not collected at Station 1. All curve fits had an $R^2 > 0.9$.

4 Discussion

As expected, our continuous underway measurements revealed strong spatial and temporal variability in biogeochemical properties across the California Upwelling system. In particular, we observed large diel cycles, and coastal-offshore gradients in biogeochemical properties, with two distinct upwelling filaments in the vicinity Cape Mendocino and Cape Blanco. Differences in nutrient availability between sample sites appeared to exert a strong influence on photo-physiology, gross photochemistry, gross primary productivity and net community productivity. In this section, we explore the potential underlying causes of biogeochemical differences across our survey region, with a focus on iron gradients across the two distinct upwelling filaments. We also discuss the direct and indirect influence of iron availability and other environmental variables on phytoplankton photo-physiology, and energy transfer efficiencies between photosynthetic processes.



4.1 Factors driving the contrasting biogeochemistry of Cape Blanco and Cape Mendocino filaments

The significant differences in surface oceanographic conditions between upwelling filaments may have been driven by differences in 1) the strength and timing of upwelling at the two Capes, or 2) differences in the nutrient content of the sub-surface upwelling source waters. We investigated these two possibilities by examining the NOAA coastal upwelling transport index (CUTI) as a proxy for upwelling strength during and prior to the sampling period, and by evaluating nutrient depth profiles to examine the upwelling source waters at the two capes. Our analysis suggests that both factors likely contributed to the apparent differences between Cape Blanco and Cape Mendocino biogeochemistry, providing evidence that Fe and Si concentrations were particularly affected by bathymetric features that influence Fe supply.

495

500 4.1.1 Strength of upwelling and relative age of filaments

To examine differences in the timing and strength of upwelling between the two filaments, we tracked CUTI for a 10 day interval prior to sampling (Jacox *et al.*, 2018). Throughout the sampling period, the strength of upwelling at Cape Blanco varied from 1.3 to 2.4 m d⁻¹ of vertical transport (positive values indicate upwelling) and peaked 6 days prior to our arrival, when vertical transport rates were 3.8 m d⁻¹. During our sampling period at Cape Mendocino, vertical transport varied from - 505 0.2 to 3.3 m d⁻¹. Upwelling conditions persisted in this region, with vertical transport rates > 2 m d⁻¹ between June 1 and 4, four to one days prior to our arrival. However, after June 4, the vertical mixing index at Cape Mendocino rapidly reversed to weak downwelling (-0.1 to -0.3 m d⁻¹) during the last few days of sampling, emphasizing the dynamic nature of this sampling environment. These results support the hypothesis that colder and more nutrient rich water near Cape Blanco was attributable 510 to stronger and more consistent upwelling in this region in the interval prior to our sampling. In contrast, Cape Mendocino was transitioning from upwelling to downwelling during our sampling period.

510

4.1.2 Nutrient Content of upwelling source waters

Nutrient depth profiles offer additional insight into the nutrient concentrations of upwelling filament source waters. Unfortunately, nutrient samples were only collected down to the base of the euphotic zone, missing the deeper source waters. Nonetheless, measurements at the base of the euphotic zone (40-50m) enable us to compare subsurface nutrient concentrations. 515 Mean concentrations of $[\text{NO}_2^- + \text{NO}_3^-]$ between 40 and 50m were significantly ($p < 0.05$) higher at Cape Blanco ($24.5 \pm 4.3 \mu\text{M}$) than at Cape Mendocino ($16.5 \pm 5.7 \mu\text{M}$). Similarly, phosphate concentrations between 40-50m were significantly greater around Cape Blanco ($2.6 \pm 0.3 \mu\text{M}$) compared to Cape Mendocino ($2.1 \pm 0.4 \mu\text{M}$; $p = 0.02$). Relative to nitrate and phosphate, larger differences were observed in Fe and Si concentrations between the two capes. The 40-50m silicic acid concentration at Cape Blanco ($30.0 \pm 8.6 \mu\text{M}$) was nearly double that observed at Cape Mendocino ($16.3 \pm 8.2 \mu\text{M}$; $p << 0.01$), while, Fe concentrations between 40-50m at Cape Blanco ($6.8 \pm 4.1 \text{nM}$) were more than three-fold higher than those at Cape Mendocino ($1.8 \pm 2.3 \text{nM}$; $p = 0.01$). These results support the hypothesis that the two upwelling plumes were seeded by different water masses with distinct nutrient concentrations.

520

Differences in underlying bathymetric features between Cape Blanco and Mendocino likely contributed to the observed 525 differences in Fe and Si availability. Cape Blanco sits over a broad section of the continental shelf (> 30km wide) composed of highly erodible sedimentary rocks with mineral rich sand-silt layers originating from the Klamath Mountains (Spigai, 1971). The broad shelf continues south until the triple junction of the North American, Pacific, and Gorda plates which forms the submarine Mendocino escarpment, a narrow ridge extending west from Cape Mendocino along the transform fault (Menard and Dietz, 1952). Importantly, the shelf rapidly narrows to less than 5 km at the latitude of Cape Mendocino (Appendix 1). 530 Differences in shelf width have important implications on sub-regional iron availability. Previous work by Biller *et al.* (2013) demonstrated that shelf width correlated with greater Fe bioavailability in the water layer directly overlying the seafloor. This trend was evident in our study as well, with a $\rho = 0.57$ correlation between shelf width and Fe concentrations at the bottom of the euphotic zone for on-shelf stations. Yet, with only nine stations on-shelf stations, this correlation was not statistically significant.



535

In contrast with NO_3^- and PO_4^{3-} , which are resupplied to the surface by upwelling, remineralized Fe is rapidly removed from the water column, such that Fe supply to the surface can be significantly decoupled from macronutrients (King and Barbeau, 2011; Bruland, Middag and Lohan, 2014). As a result, differences in upwelling strength at Cape Blanco and Cape Mendocino likely account for the differences in PO_4^{3-} and NO_3^- between the two sites, while contrasting shelf features can explain the 540 larger differences in Fe availability. These observations fit within the theory that the California Current contains a ‘mosaic’ of Fe limitation, where patches of Fe-poor water may persist even in the presence of upwelling conditions (Hutchins *et al.*, 1998; Till *et al.*, 2019). In the following section, we present several lines of evidence that photo-physiological properties of phytoplankton assemblages were influenced by iron gradients.

4.2 Environmental and taxonomic influences on physiology and productivity

545 Environmental gradients exert strong effects on physiology and productivity by determining the supply of essential nutrients that support phytoplankton growth and the maintenance of photosynthetic proteins. As a cofactor in many biological redox reactions, Fe plays a particularly important role in the photosynthetic electron transport chain and nutrient uptake pathways. Several lines of evidence suggest that iron stress was a key factor shaping phytoplankton productivity and photo-physiology 550 across our study site. As noted above, there was a significant difference in Fe concentrations between Cape Blanco (high Fe) and Mendocino (low Fe) associated with variability in the shelf width. The difference in Fe-availability was strongly correlated with $\text{Si}:\text{NO}_3^-$ ($\rho = 0.85$, $p << 0.01$), likely reflecting excess Si uptake by iron-limited diatoms (M. Franck *et al.*, 2000; Sarthou *et al.*, 2005). Further evidence of Fe-stress at Cape Mendocino was obtained from ancillary transcriptomic analysis, which 555 demonstrated elevated expression of the Fe assimilation gene *Feal* (Appendix 3), which has previously been cited as a marker of Fe-stress (Allen *et al.*, 2007). Together, these observations indicate the onset of Fe stress at sites with reduced Fe-availability. Below we outline the apparent taxonomic and physiological responses to apparent Fe stress.

560 Beyond directly affecting phytoplankton physiology, Fe gradients can indirectly influence phytoplankton physiology and productivity by driving taxonomic shifts towards species that are adapted to low Fe conditions. After chlorophyll, the second most abundant pigment across the cruise track was diatom-specific fucoxanthin, indicating that our sampling region was dominated by diatoms (Appendix 2). Microscope cell counts confirmed that diatoms were the most abundant taxa, with the majority of cells belonging to the genus *Chaetoceros*. Although diatoms were the most dominant group across the study area, their relative contribution was significantly lower around Cape Mendocino compared to Cape Blanco. Moreover, we observed a taxonomic shift towards smaller phytoplankton around Cape Mendocino, including smaller diatoms and dinoflagellates. 565 Smaller cells sizes afford larger surface area to volume ratios, facilitating nutrient uptake at lower concentrations (Sunda and Huntsman, 1997). Stations near Cape Mendocino were characterized by high abundances of *Pseudo-nitzschia*, which were absent from Cape Blanco. *Pseudo-nitzschia* is a well-studied diatom with a number of physiological adaptations to Fe-limitation, causing it to be favoured over other diatoms under low Fe conditions (Lampe *et al.*, 2018). These shifts in phytoplankton assemblages towards smaller sizes and low Fe specialists suggest bottom-up environmental controls driving taxonomic composition.

570

Cell size and nutrient status influence the optical properties and photo-physiology of phytoplankton. Large cells are prone to pigment packaging effects, which decrease Chl-specific absorption as intracellular Chl concentrations increase and surface area to volume ratios decrease. This effect causes reduced σ_{PSII} , as was observed near Cape Blanco (Table 1). Nutrient limitation, particularly for Fe, is associated with photo-inactive or damaged RCII (Roncel *et al.*, 2016). Inactive RCII still 575 absorb light, but do not contribute to photochemistry. This, in turn, drives high σ_{PSII} , which is proportional to the light harvesting complex absorption coefficient normalized by active RCII concentrations (Oxborough *et al.*, 2012; Li *et al.*, 2021), and low Fv/F_M , due to inactive RCII contributing to the F_M but not Fv signal (Schuback, Philippe D Tortell, *et al.*, 2021). Both of these commonly cited indicators of Fe stress were observed around Cape Mendocino and also offshore (Table 1).

580

The taxonomic and nutrient-dependent effects on photo-physiology described above are expected to directly impact ETR_{PSII} (Eq. 1). Previous studies have noted higher ETR_{PSII} among Fe-limited phytoplankton, presumably due to increased σ_{PSII}



(Schuback *et al.*, 2015). However, we observed greater ETR_{PSII} in the relatively Fe-rich waters near Cape Blanco (Table 1), likely due to high $F'_q/F'_v(PAR)$, which represents the proportion of open RCII at a given light level (Suggett, Moore and Geider, 2011). Low NPQ observed in the Cape Blanco region (Fig. 4d) likely enabled F'_q/F'_v to remain high under high light levels. It is well recognized that iron limitation exacerbates high light stress and NPQ (Ryan-keogh *et al.*, 2020; Schallenberg *et al.*, 2020), and the high NPQ at Cape Mendocino compared to Cape Blanco provides further evidence that Cape Mendocino assemblages were affected by Fe stress. Iron limitation can also impact photosynthetic processes downstream of ETR_{PSII} . In this study, maximum carbon fixation rates (P_{max} determined during ^{14}C PI experiments) displayed a strong correlation with Si ($\rho = 0.63$, $p << 0.01$) and the ratio of Si:NO₃⁻ ($\rho = 0.60$, $p << 0.01$) in the water column.

585

590

595

Overall, our results suggest that Fe availability gradients between Cape Blanco and Mendocino influenced local community composition and physiology with consequential effects on C and Si cycles. Differences in taxonomic composition, photo-physiology, nutrient quotas and productivity all serve as evidence that the community shifted towards Fe-limitation in proximity to Cape Mendocino. Due to the differential sensitivity of ETR_{PSII} , carbon fixation, and NCP to Fe-availability, we hypothesized that Fe-limitation would lead to a decoupling between these different PP currencies. We explore this hypothesis below with direct comparisons of ETR_{PSII} , C-fixation, and NCP.

4.3 Energy transfer efficiencies between photosynthetic processes

600

605

610

Measurements of primary productivity in different ‘currencies’ (carbon, oxygen and electrons) each reflect the rates of different photosynthetic processes. Comparison of these alternative productivity metrics thus yields information on energy transfer efficiencies across different components of the photosynthetic pipeline (Fig 7). Theoretically, water-splitting and carbon fixation have fixed stoichiometries, with 4 charge separation events required to produce one O₂ and fix one CO₂. Yet a number of non-linear electron transport pathways divert reducing power from carbon fixation, decoupling ETR_{PSII} from GPP (Fig 7). Oxygen consumption by respiration and non-linear electron transport pathways further decouple ETR_{PSII} from O₂ fluxes and NCP. The ratio between ETR_{PSII} and GPP thus provides information on the magnitude of non-linear electron transport, while the ratio between ETR_{PSII} and NCP reflects the sum of non-linear electron transport and respiration. In practice, interpreting apparent decoupling between ETR, GPP, and NCP is complicated by differences in the temporal and spatial scales captured by different measurement approaches, as well as the various assumptions implicit in each method. In the following sections, we directly compare parallel productivity measurements to examine energy transfer efficiencies across photosynthetic processes, taking care to note important methodological considerations.

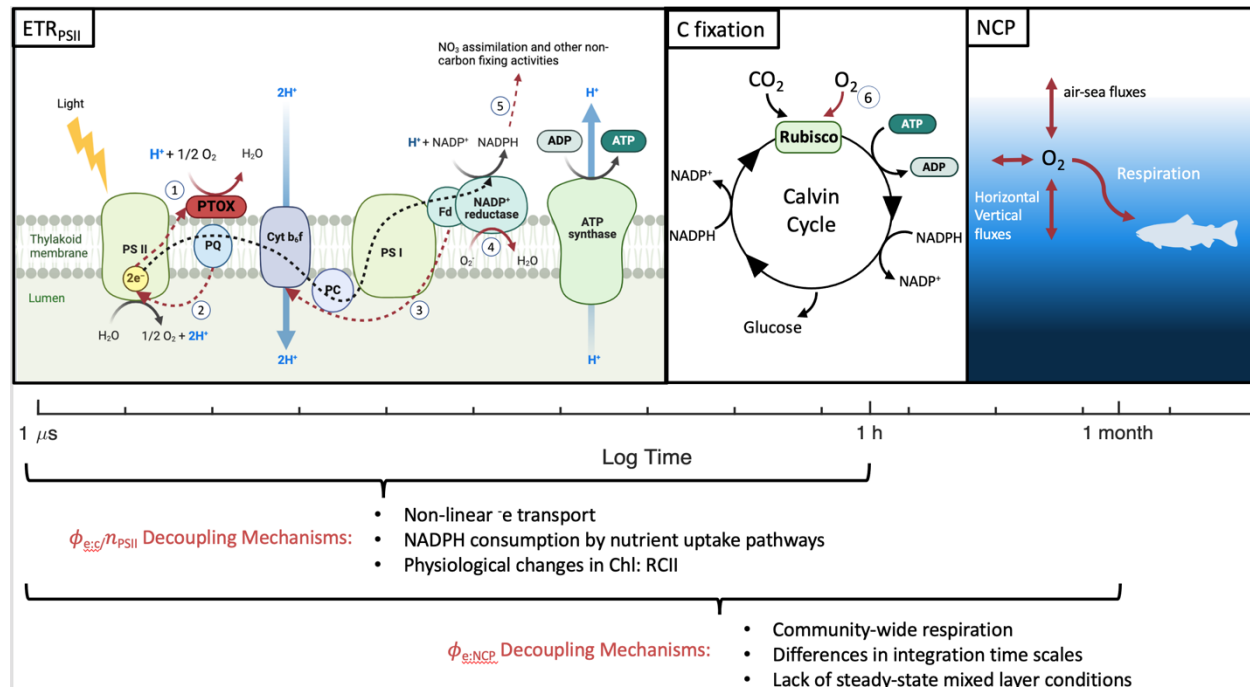


Figure 7. Different primary productivity currencies and their decoupling mechanisms. The three productivity currencies of interest are indicated with respect to the spatial times scales they represent. Numbered red pathways denote decoupling mechanisms including 1) photorespiration 2) cyclic transport around PSII 3) cyclic transport around PSI 4) pseudo-cyclic/ Mehler reactions 5) reductant consuming nutrient uptake pathways 6) chloro-respiration and 7) Community-wide respiration. Figure produced in Biorender.

4.3.1 Carbon fixation as a function of ETR_{PSII}

Non-linear electron transport pathways (Fig 7) maintain redox homeostasis when ETR_{PSII} exceeds downstream energy requirements for growth and metabolism. The energy balance between PSII and PSI becomes disrupted under high irradiance, when PSII absorbs energy in excess of PSI electron transport rates, and/or under nutrient limitation, limiting the synthesis of electron transporters (Schuback, Schallenberg, Duckham and Maldonado, 2015; Roncel *et al.*, 2016; Hughes, Varkey, *et al.*, 2018). Iron limitation, in particular, exerts acute constraints on the synthesis of Photosystem I (PSI) and Cytochrome b₆f (Cyt b₆f), which require 12 and 5 Fe atoms each (Raven, Evans and Korb, 1999). As a result, Fe-limited phytoplankton have high levels of PSII relative to PSI, exacerbating energy imbalances between PSII and PSI, and necessitating upregulation of non-linear electron transport pathways (Behrenfeld and Milligan, 2013). We therefore hypothesized that Fe-stress would increase decoupling between C-fixation and ETR_{PSII}.

One of the primary findings of this work is that C-fixation varies as a hyperbolic function of ETR_{PSII}. Curve shapes, defined by the maximum carbon fixation rate (P_{max-C}) and the saturation constant (K_{sat}), were highly variable between samples (Fig. 6). Samples with high P_{max-C} and K_{sat} , (e.g. Station 6) showed more linear relationships between C-fixation and ETR_{PSII}, and had a nearly constant electron requirement for carbon fixation ($\phi_e: c/n_{PSII}$, units = 'e Chl C⁻¹ RCII⁻¹), indicating tightly coupled ETR_{PSII} and carbon fixation (Fig 8). By contrast, in samples with low P_{max-C} and K_{sat} , carbon-fixation quickly saturated with respect to ETR_{PSII}, resulting in an increase in $\phi_e: c/n_{PSII}$ with increasing light levels (e.g. Station 7). Determining sources of P_{max-C} and K_{sat} variability therefore provides significant utility in predicting the stoichiometry of electron requirements for



gross carbon fixation. This stoichiometry, represented by $\phi_e:c/n_{PSII}$, is necessary to derive GPP in ecologically-relevant carbon units from fluorescence-based ETR_{PSII} measurements.

Previous studies have documented the importance of different environmental, taxonomic and physiological parameters in driving variability in $\phi_e:c/n_{PSII}$, but efforts to develop empirical algorithms predicting $\phi_e:c/n_{PSII}$ remain ongoing. Recent studies have used NPQ_{NSV} to predict $\phi_e:c/n_{PSII}$, based on the rationale that NPQ responds directly to excess excitation pressure, which is also expected to stimulate non-linear electron transport. Recently, Schuback *et al.*, (2015, 2016, 2017) noted a consistent relationship between NPQ_{NSV} and $\phi_e:c/n_{PSII}$ in the surface waters of the Northeast Pacific and Canadian Arctic, suggesting that carbon fixation can be estimated using FRRF-based NPQ and ETR_{PSII} measurements alone. Subsequent studies have applied the $NPQ_{NSV} \propto \phi_{e:c}/n_{PSII}$ relationship observed by Schuback *et al.* (2015) to collect high-resolution fluorescence-based GPP estimates, e.g. Kranz *et al.* (2020). Others, however, have noted that the $NPQ_{NSV} \propto \phi_{e:c}/n_{PSII}$ relationship does not hold for all taxa (Hughes *et al.*, 2021), light conditions (Schuback *et al.*, 2017), or environments where phytoplankton grow on more reduced N forms like NH_4^+ (Fei *et al.*, 2024).

In our study, NPQ_{NSV} was positively correlated with $\phi_{e:c}/n_{PSII}$ ($\rho = 0.55, p < 0.01$). However, the linear relationship proposed by Schuback *et al.* (2017; 2019) did not adequately predict $\phi_{e:c}/n_{PSII}$ for our samples ($R^2 = -0.41$), nor did we find a single line of best fit that could describe all of our data ($R^2 = 0.30$). Rather, we found that $\phi_{e:c}/n_{PSII}$ scaled directly with NPQ_{NSV} only for samples with low C_{max} ($\leq 0.3 \text{ C Chl}^{-1} \text{ s}^{-1}$). In contrast, for samples with high P_{max-C} ($> 0.3 \text{ C Chl}^{-1} \text{ s}^{-1}$), $\phi_{e:c}/n_{PSII}$ remained relatively constant across increasing light, NPQ_{NSV} , and ETR_{PSII} (Fig 8).

|655

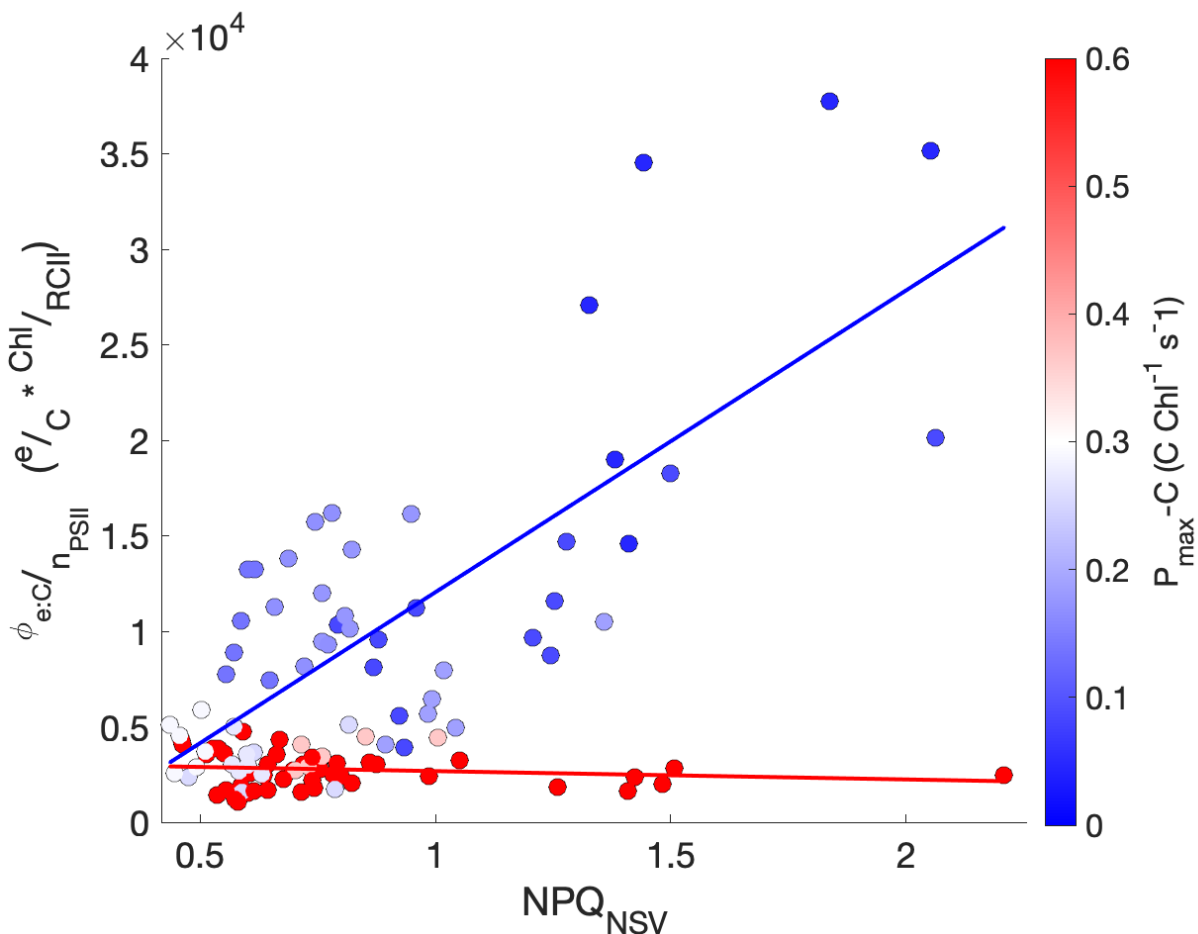




Figure 8. The relationship between $\phi_{e:C}$, NPQ_{NSV} and V_{max}. Lines of best fit are drawn through points with P_{max-C} <= 0.3 and > 0.3 mol C mol Chl⁻¹ s⁻¹, with the colorbar indicating P_{max-C}.

660 The hyperbolic function used to fit ETR_{PSII} and carbon fixation data is equivalent to the Michaelis-Menten equation commonly used to describe enzyme kinetics data. By analogy with the enzyme kinetics model, variability in P_{max-C} can be explained as the product of the enzyme concentration and maximum reaction rate (Choi, Rempala and Kim, 2017). In our case, P_{max-C} reflects the entire suite of proteins that facilitate the conversion of chemical energy to organic matter. Reduced concentrations of PSI and Cyt b₆f expected under Fe-stress would therefore reduce P_{max-C}. Consistent with this hypothesis, V_{max} was
665 significantly correlated to physiological markers of Fe-stress, σ_{PSII} ($\rho = -0.68$, $p << 0.01$), Fv/Fm ($\rho = 0.56$, $p = 0.02$), and Si:NO₃⁻ ($\rho = 0.60$, $p = 0.01$). Additionally, meta transcriptomic analysis of diatom RNA revealed significant positive correlations ($p < 0.05$) between P_{max-C} and the expression level of different PSI subunits (*psaE*, *psaL*, *psaM*), with correlation coefficients of $\rho = 0.71$, 0.70 , and 0.93 , respectively. In contrast, there were no detected correlations between P_{max-C} and Cyt b₆f, however Cyt b_{559a}, a subunit of PSII thought to be involved in photoprotection (Burda *et al.*, 2003), also demonstrated a
670 strong positive correlation with P_{max-C} ($\rho = 0.76$, $p < 0.05$).

In addition to non-linear electron transport, $\phi_{e:C}/n_{PSII}$ is also affected by the number of Chl energetically coupled to RCII. Without directly measuring Chl:RCII, which requires either an FRRF instrument-specific calibration factor or specialized O₂ flash yield instrumentation, it is challenging to isolate the drivers of $\phi_{e:C}/n_{PSII}$ variability (Oxborough *et al.*, 2012; Xu *et al.*, 675 2018). Yet, Chl:RCII is known to be sensitive to iron and light availability (Greene *et al.*, 1992; Murphy *et al.*, 2017). Although low light acclimated phytoplankton can increase Chl:C to maximize light absorption (Geider, 1987), we did not note a strong correlation between the light-acclimation parameter E_K and V_{max} ($\rho = -0.21$, $p >> 0.05$), indicating that differences in light acclimation state was not a primary driver of electron-carbon ratios in our study area. Iron limitation is also expected to increase Chl:RCII, because although iron limitation lowers cellular Chl content, and Chl is more likely to be energetically coupled to 680 RCII rather than PSI reaction centers (Greene *et al.*, 1992). We thus conclude that Fe-stress likely contributed to variability in $\phi_{e:C}/n_{PSII}$ by driving increases Chl:RCII in addition to influencing non-linear electron transport rates.

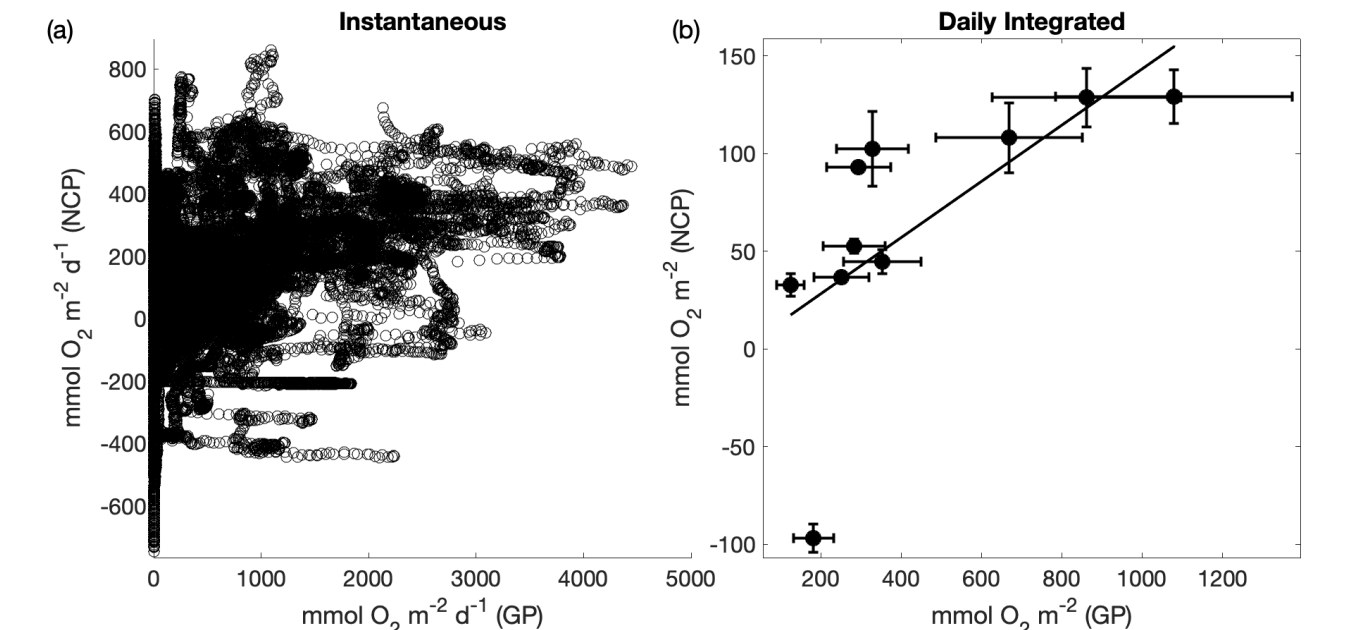
4.3.2 Comparison of ETR_{PSII} and NCP

As opposite end members of the productivity spectrum (Fig. 7), ETR_{PSII} quantifies gross photochemical energy production, 685 while NCP represents the net accumulation of photosynthetic carbon or oxygen remaining after accounting for all sources of mixed layer respiration. To directly compare ETR_{PSII} and NCP, we converted ETR_{PSII} from units of e⁻ RCII⁻¹ s⁻¹ to mmol O₂ m⁻² d⁻¹ (Eq. 5) by assuming each RCII was functionally coupled to 400 – 700 Chl pigments (Kolber and Falkowski, 1993; Schuback, Schallenberg, Duckham and Maldonado, 2015) and 4 charge separation events per gross O₂ evolved. The resulting O₂-based gross photochemistry values varied between 0 – 4000 mmol O₂ m⁻² d⁻¹ (Fig. 5c), within range of previously reported 690 values for the CCS (Kranz *et al.*, 2020). On average, NCP accounted for 17 \pm 8% of gross photochemistry, indicating ~80% of oxygen produced at PSII by water splitting reactions was consumed within the mixed layer through autotrophic and heterotrophic respiration. In contrast to $\phi_{e:C}/n_{PSII}$, there was no significant differences in NCP:ETR_{PSII} between Cape Blanco, Cape Mendocino, or offshore. Although NCP is constrained by gross photochemistry, NCP was greater than ETR_{PSII} over 29% of the cruise track. This apparent contradiction can be explained by differences time-scales between instantaneous ETR_{PSII} 695 measurements, and NCP, which is integrated over O₂ residence times in the mixed layer (~1–2 weeks). Sustained net autotrophy can lead to accumulation of O₂ in the mixed layer, such that measured O₂ fluxes indicate high levels of NCP despite short-term decreases in ETR_{PSII} (e.g. overnight).

Regardless of the large differences in integration time-scales and metabolic sources of decoupling, NCP showed strong 700 coherence with ETR_{PSII} (Fig 9). Direct comparison between continuous underway measurements of ETR_{PSII} and NCP yielded a moderate positive correlation ($\rho = 0.43$, $p << 0.01$). To account for some of the decoupling introduced by the strong diel dependence of ETR_{PSII}, we also compared ETR_{PSII} and NCP measurements integrated over 24hr bins. This comparison indicated a much stronger relationship between ETR_{PSII} and NCP ($\rho = 0.92$, $p << 0.01$; Fig 9). Across daily integrated time-scales, NCP linearly increased as a function of ETR_{PSII} with a ~15% energy transfer efficiency and a predicted NCP of -0.55



705 mmol O₂ m⁻² when ETR_{PSII} is zero. This efficiency estimate is within range of previous studies that have compared gross oxygen production and NCP using triple oxygen isotope and O₂/Ar methods (Haskell II *et al.*, 2017; Howard *et al.*, 2017), despite the differences in integration time scales between ETR and the triple oxygen isotope method. Further, a sensitivity analysis found no significant changes in the derived energy transfer efficiency between ETR and NCP integrated over 24, 48, 72, and 96-hour bins. These results suggest the utility of FRRF to 1) estimate gross oxygen productivity as an alternative to triple oxygen isotopes or other discrete methods (e.g. H₂¹⁸O tracer experiments), and 2) constrain net community productivity estimates.



715 **Figure 9. Comparison between fluorescence-based gross photochemistry (GP) and NCP.** The left subpanel directly compares continuous underway ETR_{PSII} and NCP measurements ($\rho = 0.43$, $p << 0.01$), while the right panel compares daily-integrated measurements of ETR_{PSII} and NCP measurements ($\rho = 0.92$, $p << 0.01$). A line of best fit ($y = 0.14*GP - 0.55$) is drawn through the positive NCP data points. The error bars represent the total uncertainty of each measurement determined by propagating uncertainty in each input variable. For GPP, total uncertainty is dominated by uncertainty in the Chl:RCII, while for NCP, major sources of uncertainty include uncertainty in the deep water supply ratio of O₂:N₂O, and modelled differences between [N₂] and [Ar]. Assumption biases (e.g. no horizontal advection of O₂) also represents a potential large source of uncertainty but was not quantified. A line of best fit is drawn through the positive NCP points on the right plot with the equation $y = 0.14 * GPP - 0.55$ ($R^2 = 0.82$).

5 Conclusion

725 Consistent with previous observations, our results indicate a patchwork of Fe-stress within the coastal upwelling waters of the California Current, providing evidence for physiological Fe-stress within an upwelling filament near Cape Mendocino. Differences in iron availability between upwelling filaments appear to be linked to bathymetric features that influence sediment loading, and variable micronutrient content of sub-surface upwelling source waters. Paired fluorescence- and ¹⁴C-based photosynthesis-irradiance measurements indicated strong connectivity between ETR_{PSII} and carbon-fixation in Fe-replete phytoplankton, and greater decoupling in these rates for Fe-limited assemblages, with greater associated variability in $\phi_e:C/n_{PSII}$. Recently, there has been significant focus on understanding $\phi_e:C/n_{PSII}$ variability to expand FRRF-based GPP surveys (Hughes, Campbell, *et al.*, 2018). Our results suggest that nutrient replete phytoplankton are able to maintain near

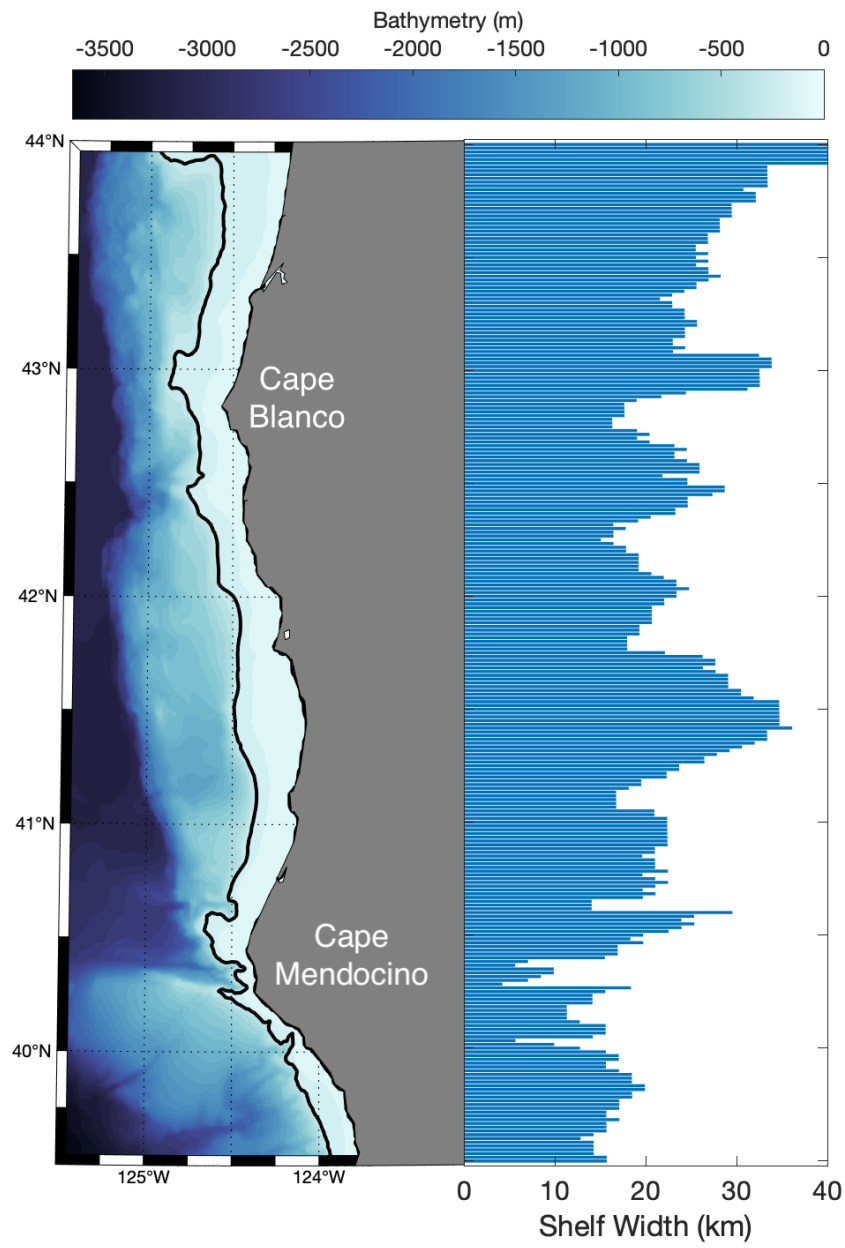


constant $\phi_e: C/n_{PSII}$ under increasing excitation pressures due to their ability to efficiently transfer energy between PSI and PSII. Under these circumstances, NPQ_{NSV} is not a good predictor of $\phi_e: C/n_{PSII}$. However, where nutrient limitation necessitates enhanced non-linear electron transport pathways to maintain energy balance between PSII and PSI, $\phi_e: C/n_{PSII}$ does scale with NPQ_{NSV} and excess excitation pressure. With the accumulation of further data across a range of oceanographic conditions, it may be possible to derive more robust empirical relationships between NPQ_{NSV} and $\phi_e: C/n_{PSII}$, which could be used to derive GPP in C-based units from FRRF measurements. In addition, our results show a strong general coherence between daily integrated ETR_{PSII} and NCP measurements, suggesting that ETR_{PSII} may have significant utility as an indicator of bulk primary productivity. We thus conclude that high-resolution, ship-board measurements hold significant potential to explore fine-scale variability in surface water primary productivity in complex coastal waters.

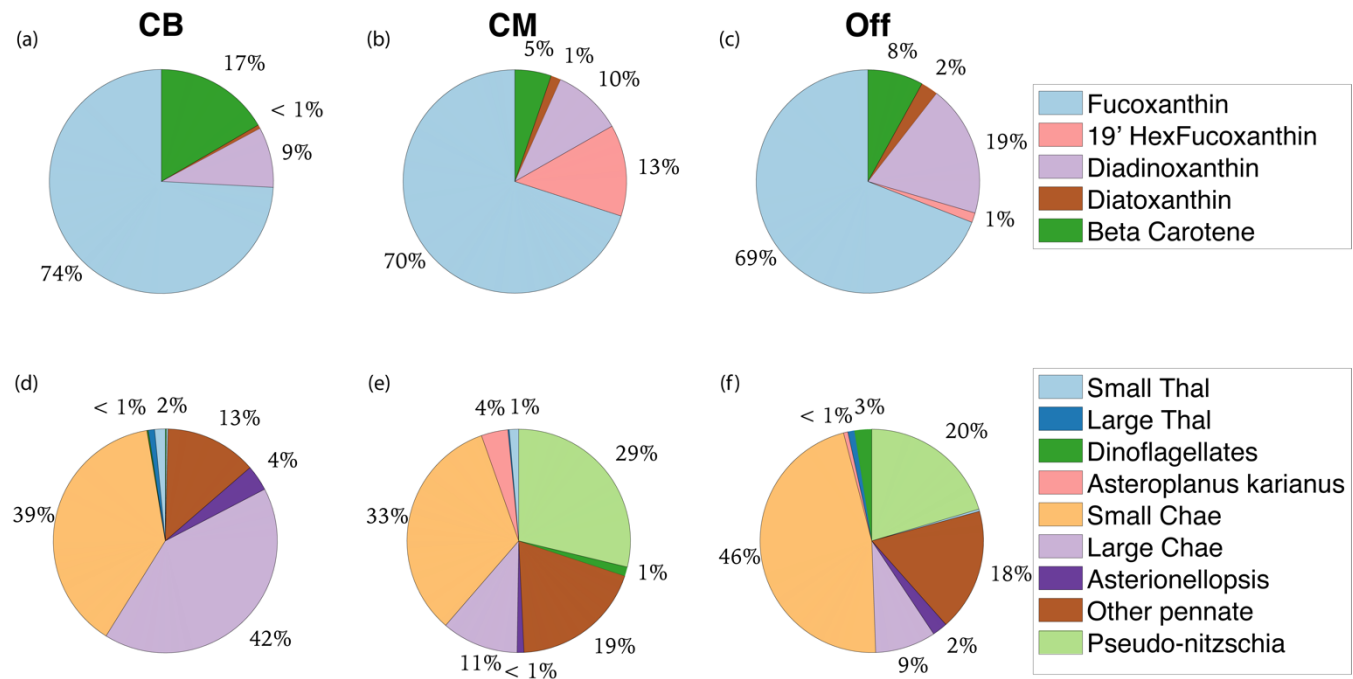
735



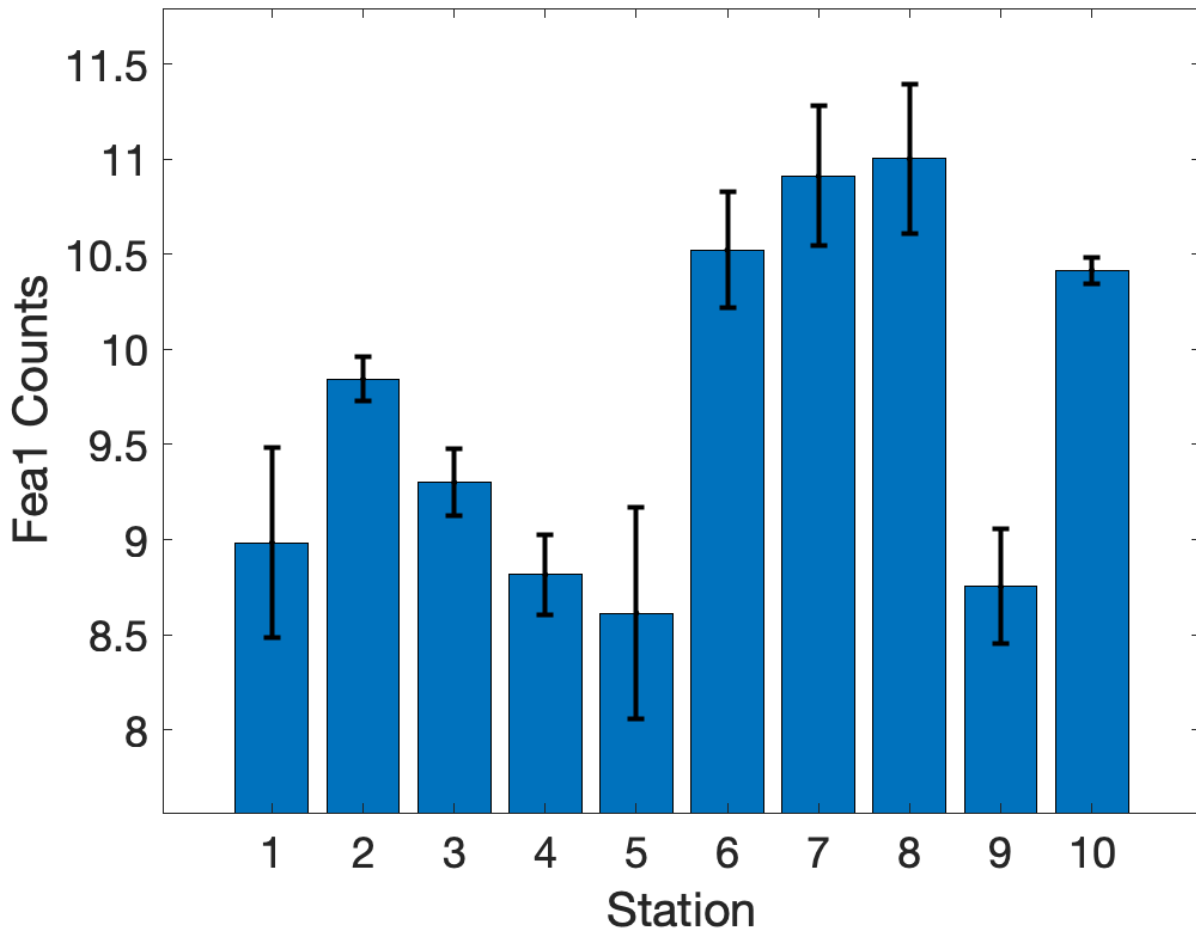
740 6 Appendix



Appendix 1. Bathymetric map of the study region. The black contour line indicates the 200m isobath. The horizontal bar graph demonstrates the shelf width at the aligned latitude.



Appendix 2. Pigment and taxonomic composition of study area sub-regions. a-c) display non-Chl pigment distribution by mass for Cape Blanco (CB), Cape Mendocino (CM), and Offshore (Off). d-f) display the taxonomic distribution of diatom and dinoflagellate groups visible for microscope counts.



Appendix 3. Diatom-specific expression of Fe assimilation gene *Fea1*. Bar height displays *Fea1* count means by station. Error bars display the standard deviation. Stations 1–4 were in close proximity of Cape Blanco, 6 and 10 were offshore while the remaining stations were in proximity of the Cape Mendocino upwelling filament.

755 7 Code and data availability

In-situ hydrographic, dissolved gas concentration, and phytoplankton photophysiology data collected during the PUPCYCLE II expedition have been submitted to PANGAEA, an Earth Science data repository, and are being tracked with the submission codes PDI – 39901, 39902, and 39930, respectively. Dissolved Fe data have been submitted to <https://www.bco-dmo.org/>. DOI names are expected to be issued shortly. Satellite SST (11 μ daytime) and Chl data used to produce Fig 1 were downloaded from NASA Aqua MODIS platform (<https://oceancolor.gsfc.nasa.gov/l3/>). Ancillary data required to derive N₂' were sourced from several public databases. Wind speed and Ekman transport were taken from NOAA's Windspeed, Stress, Curl, Divergence, and Ekman Upwelling, Metop-C ASCAT, 0.25 degree, Global, Near Real Time, 2020–present, 1-Day Composite product. Sea level pressure was downloaded from the US Navy Global Environmental Model (NAVGEM) 0.5 degree, 2013–present Pressure MSL



765 (https://coastwatch.pfeg.noaa.gov/erddap/griddap/erdNavgem05DPres.html). Modeled sea surface temperature and salinity products were downloaded from <https://psl.noaa.gov/data/gridded/data.noaa.oisst.v2.highres.html> and https://podaac.jpl.nasa.gov/dataset/SMAP_JPL_L3_SSS_CAP_8DAY-RUNNINGMEAN_V5, respectively. Model code used to calculate N₂' and NCP calculations are available at https://github.com/rizett/O2N2_NCP_toolbox.

8 Author Contributions

770 Y.S. conceived the research plan, conducted FRRF and ¹⁴C measurements, analysed data and wrote the manuscript with significant contribution from all co-authors. K.S. operated the PIGI, conducted all N₂O measurements, and assisted with NCP computations and analysis. E.S. collected macronutrient and meta-transcriptomic data and assisted with meta-transcriptomic analysis. A.M. facilitated meta-transcriptomic data collection, assisted with meta-transcriptomic analysis, and co-organized the PUPCYCLE II expedition with C.T. Trace metal clean Fe samples were collected by C.T. and processed by R.T. Funding 775 was secured by A.M., C.T., and P.T. Primary advisory support and manuscript editing was done by P.T.

9 Competing Interests

The authors declare they have no conflict of interest.

10 Acknowledgements

780 We would like to thank the crew and fellow scientists aboard the *R/V Sally Ride* who made this work possible and created a delightful working environment. Special thanks to Sacchinandan Pillai who provided HPLC data and mobilization assistance. We thank the Bundy lab at the University of Washington for the loan of their trace metal sampling van. We thank D. Patel from the University of North Carolina for performing microscope counts.

11 Financial Support

785 Funding for the PUPCYCLE II cruise was provided to AM from a National Science Foundation grant (OCE1751805). Iron analyses were funded through the Research Corporation for Science Advancement's Cottrell Scholar Award #26844 to C.T. Trace metal sampling was conducted with a shared-use rosette maintained at Skidaway and purchased with NSF Award OCE-2015430.

12 References

790 Aardema, H. M. *et al.* (2024) 'On the Variability of Phytoplankton Photophysiology Along a Latitudinal Transect in the North Atlantic Surface Ocean', *Journal of Geophysical Research: Biogeosciences*, 129(9), p. e2023JG007962. doi: <https://doi.org/10.1029/2023JG007962>.

795 Allen, M. *et al.* (2007) 'FEA1, FEA2, and FRE1, encoding two homologous secreted proteins and a candidate ferrireductase, are expressed coordinately with FOX1 and FTR1 in iron-deficient *Chlamydomonas reinhardtii*', *Eukaryot Cell*. doi: 10.1128/EC.00205-07.

Andrews, S. (2010) 'FastQC: a quality control tool for high throughput sequence data.'

Austin, J. A. and Barth, J. A. (2002) 'Variation in the position of the upwelling front on the Oregon shelf', *Journal of*



Geophysical Research: Oceans, 107(C11), pp. 1–15. doi: <https://doi.org/10.1029/2001JC000858>.

800

Balch, W. M. *et al.* (2021) ‘Ocean Optics & Biogeochemistry Protocols for Satellite Ocean Colour Sensor Validation IOCCG Protocol Series Volume 7 .0 , 2021 Aquatic Primary Productivity Field Protocols for Satellite Validation and Model Synthesis (DRAFT) Report of a NASA-sponsored ’, 7.

805

Banse, K. (2002) ‘SHOULD WE CONTINUE TO MEASURE ^{14}C -UPTAKE BY PHYTOPLANKTON FOR ANOTHER 50 YEARS?’, *Limnology and Oceanography Bulletin*, 11(3), pp. 45–46. doi: <https://doi.org/10.1002/lob.200211345>.

Behnke, J. and LaRoche, J. (2020) ‘Iron uptake proteins in algae and the role of Iron Starvation-Induced Proteins (ISIPs)’, *European Journal of Phycology*. Taylor & Francis, 55(3), pp. 339–360. doi: 10.1080/09670262.2020.1744039.

810

Behrenfeld, M. J. *et al.* (2005) ‘Carbon-based ocean productivity and phytoplankton physiology from space’, *Global Biogeochemical Cycles*, 19(1), pp. 1–14. doi: 10.1029/2004GB002299.

815

Behrenfeld, M. J. and Falkowski, P. G. (1997) ‘Photosynthetic rates derived from satellite-based chlorophyll concentration’, *Limnology and Oceanography*, 41(January), pp. 1–20. Available at: <https://www.google.com/search?q=Engle+et+al.+%2C2000&oq=Engle+et+al.+%2C2000&aqs=chrome..69i57.11777j0j8&sourc eid=chrome&ie=UTF-8>.

820

Behrenfeld, M. J. and Milligan, A. J. (2013) ‘Photophysiological expressions of iron stress in phytoplankton’, *Annual Review of Marine Science*, 5, pp. 217–246. doi: 10.1146/annurev-marine-121211-172356.

Biller, D. V *et al.* (2013) ‘Coastal iron and nitrate distributions during the spring and summer upwelling season in the central California Current upwelling regime’, *Continental Shelf Research*, 66, pp. 58–72. doi: <https://doi.org/10.1016/j.csr.2013.07.003>.

825

Bograd, S. J. *et al.* (2023) ‘Climate Change Impacts on Eastern Boundary Upwelling Systems’, *Annual Review of Marine Science*, 15, pp. 303–328. doi: 10.1146/annurev-marine-032122-021945.

830

Bruland, K. W. *et al.* (2005) ‘Iron, macronutrients and diatom blooms in the Peru upwelling regime: brown and blue waters of Peru’, *Marine Chemistry*, 93(2), pp. 81–103. doi: <https://doi.org/10.1016/j.marchem.2004.06.011>.

Bruland, K. W., Middag, R. and Lohan, M. C. (2014) ‘8.2 - Controls of Trace Metals in Seawater’, in Holland, H. D. and Turekian, K. K. (eds) *Treatise on Geochemistry (Second Edition)*. Second Edi. Oxford: Elsevier, pp. 19–51. doi: <https://doi.org/10.1016/B978-0-08-095975-7.00602-1>.

835

Buchfink, B., Xie, C. and Huson, D. H. (2015) ‘Fast and sensitive protein alignment using DIAMOND’, *Nature Methods*, 12(1), pp. 59–60. doi: 10.1038/nmeth.3176.

840

Burda, K. *et al.* (2003) ‘Mössbauer studies of the non-heme iron and cytochrome b 559 in a *Chlamydomonas reinhardtii* PSI– mutant and their interactions with α -tocopherol quinone’, *FEBS Letters*, 535(1–3), pp. 159–165. doi: [https://doi.org/10.1016/S0014-5793\(02\)03895-4](https://doi.org/10.1016/S0014-5793(02)03895-4).

Bushmanova, E. *et al.* (2019) ‘RnaSPADEs: A de novo transcriptome assembler and its application to RNA-Seq data’, *GigaScience*. Oxford University Press, 8(9), pp. 1–13. doi: 10.1093/gigascience/giz100.

845

Carvalho, F. *et al.* (2020) ‘FIRE glider: Mapping in situ chlorophyll variable fluorescence with autonomous underwater gliders’, *Limnology and Oceanography: Methods*, 18(9), pp. 531–545. doi: 10.1002/lom3.10380.



850 Cassar, N. *et al.* (2009) 'Continuous high-frequency dissolved O₂/Ar Measurements by Equilibrator Inlet Mass Spectrometry', *Analytical Chemistry*, 81(5), pp. 1855–1864. doi: 10.1021/ac802300u.

855 Cassar, N., Nevison, C. D. and Manizza, M. (2014) 'Correcting oceanic O₂/Ar-net community production estimates for vertical mixing using N₂O observations', *Geophysical Research Letters*, 41(24), pp. 8961–8970. doi: <https://doi.org/10.1002/2014GL062040>.

Castelao, R. M. and Luo, H. (2018) 'Upwelling jet separation in the California Current System', *Scientific Reports*. Springer US, 8(1), pp. 1–8. doi: 10.1038/s41598-018-34401-y.

860 Choi, B., Rempala, G. and Kim, J. (2017) 'Beyond the Michaelis-Menten equation: Accurate and efficient estimation of enzyme kinetic parameters.', *Sci Rep.* doi: 10.1038/s41598-017-17072-z.

Craig, H. and Hayward, T. (1987) 'Oxygen Supersaturation in the Ocean: Biological Versus Physical Contributions', *Science*, 235(4785), pp. 199–202. doi: 10.1126/science.235.4785.199.

865 Cutter, G. *et al.* (2014) 'Sampling and sample-handling protocols for GEOTRACES cruises. GEOTRACES cookbook', (December), pp. 1–238. Available at: http://www.geotraces.org/images/stories/documents/intercalibration/Cookbook_v2.pdf.
Deutsch, C. *et al.* (2021) 'Biogeochemical variability in the California Current System', *Progress in Oceanography*, 196, p. 102565. doi: <https://doi.org/10.1016/j.pocean.2021.102565>.

870 Domingues, R. B. and Barbosa, A. B. (2023) 'Evaluating Underwater Light Availability for Phytoplankton: Mean Light Intensity in the Mixed Layer versus Attenuation Coefficient', *Water*, 15(16). doi: 10.3390/w15162966.

Elkins, J. W. *et al.* (1978) 'Aquatic sources and sinks for nitrous oxide', *Nature*, 275(5681), pp. 602–606. doi: 10.1038/275602a0.

875 Federhen, S. (2012) 'The NCBI Taxonomy database', *Nucleic Acids Research*, 40(D1), pp. D136–D143. doi: 10.1093/nar/gkr1178.

880 Fei, S. *et al.* (2024) 'The linkage between phytoplankton productivity and photosynthetic electron transport in the summer from the Changjiang River to the East China Sea', *Frontiers in Marine Science*, 11. doi: 10.3389/fmars.2024.1383988.

GEIDER, R. J. (1987) 'LIGHT AND TEMPERATURE DEPENDENCE OF THE CARBON TO CHLOROPHYLL a RATIO IN MICROALGAE AND CYANOBACTERIA: IMPLICATIONS FOR PHYSIOLOGY AND GROWTH OF PHYTOPLANKTON', *New Phytologist*, 106(1), pp. 1–34. doi: <https://doi.org/10.1111/j.1469-8137.1987.tb04788.x>.

885 Greene, R. M. *et al.* (1992) 'Iron-Induced Changes in Light Harvesting and Photochemical Energy Conversion Processes in Eukaryotic Marine Algae 1', *Plant Physiology*, 100(2), pp. 565–575. doi: 10.1104/pp.100.2.565.

890 Groussman, R. D. *et al.* (2023) 'MarFERReT, an open-source, version-controlled reference library of marine microbial eukaryote functional genes', *Scientific Data*, 10(1), p. 926. doi: 10.1038/s41597-023-02842-4.

Grundle, D. S., Juniper, S. K. and Giesbrecht, K. E. (2013) 'Euphotic zone nitrification in the NE subarctic Pacific: Implications for measurements of new production', *Marine Chemistry*, 155, pp. 113–123. doi: <https://doi.org/10.1016/j.marchem.2013.06.004>.

895 Halsey, K. H. and Jones, B. M. (2015) 'Phytoplankton Strategies for Photosynthetic Energy Allocation', *Annual Review of Marine Science*. Annual Reviews, 7(Volume 7, 2015), pp. 265–297. doi: <https://doi.org/10.1146/annurev-marine-010814-015813>.



900 Haskell II, W. Z. *et al.* (2017) 'Annual cyclicity in export efficiency in the inner Southern California Bight', *Global Biogeochemical Cycles*, 31(2), pp. 357–376. doi: <https://doi.org/10.1002/2016GB005561>.

905 Horrigan, S. G., Carlucci, A. F. and Williams, P. M. (1981) 'Light inhibition of nitrification in sea-surface films', *Journal of Marine Research*, 39. Available at: https://elischolar.library.yale.edu/journal_of_marine_research/1559.

Howard, E. M. *et al.* (2017) 'Biological production, export efficiency, and phytoplankton communities across 8000 km of the South Atlantic', *Global Biogeochemical Cycles*, 31(7), pp. 1066–1088. doi: <https://doi.org/10.1002/2016GB005488>.

910 Hughes, D. J., Varkey, D., *et al.* (2018) 'Impact of nitrogen availability upon the electron requirement for carbon fixation in Australian coastal phytoplankton communities', *Limnology and Oceanography*, 63(5), pp. 1891–1910. doi: [10.1002/lo.10814](https://doi.org/10.1002/lo.10814).

915 Hughes, D. J., Campbell, D. A., *et al.* (2018) 'Roadmaps and Detours: Active Chlorophyll- a Assessments of Primary Productivity Across Marine and Freshwater Systems', *Environmental Science and Technology*, 52(21), pp. 12039–12054. doi: [10.1021/acs.est.8b03488](https://doi.org/10.1021/acs.est.8b03488).

Hughes, D. J. *et al.* (2021) 'Taxonomic Variability in the Electron Requirement for Carbon Fixation Across Marine Phytoplankton', *Journal of Phycology*, 57(1), pp. 111–127. doi: <https://doi.org/10.1111/jpy.13068>.

920 Hutchins, D. A. *et al.* (1998) 'An iron limitation mosaic in the California upwelling regime', *Limnology and Oceanography*, 43(6), pp. 1037–1054. doi: <https://doi.org/10.4319/lo.1998.43.6.1037>.

Izett, R. W. *et al.* (2018) 'Refined Estimates of Net Community Production in the Subarctic Northeast Pacific Derived From $\Delta\text{O}_2/\text{Ar}$ Measurements With N_2O -Based Corrections for Vertical Mixing', *Global Biogeochemical Cycles*, 32(3), pp. 326–350. doi: <https://doi.org/10.1002/2017GB005792>.

925 Izett, R. W. (2021) 'Improved Estimates of Net Community Production in the Subarctic Pacific and Canadian Arctic Ocean Using Ship-Based Autonomous Measurements and Computational Approaches', (June).

930 Izett, R. W. *et al.* (2021) ' $\Delta\text{O}_2/\text{N}_2$ ' as a New Tracer of Marine Net Community Production: Application and Evaluation in the Subarctic Northeast Pacific and Canadian Arctic Ocean', *Frontiers in Marine Science*, 8(August), pp. 1–19. doi: [10.3389/fmars.2021.718625](https://doi.org/10.3389/fmars.2021.718625).

Izett, R. W. and Tortell, P. D. (2020) 'The pressure of in situ gases instrument (Pigi) for autonomous shipboard measurement of dissolved O_2 and N_2 in surface ocean waters', *Oceanography*, 33(2), pp. 156–162. doi: [10.5670/oceanog.2020.214](https://doi.org/10.5670/oceanog.2020.214).

935 Izett, R. W. and Tortell, P. D. (2021) ' $\Delta\text{O}/\text{N}$ ' as a tracer of mixed layer net community production: Theoretical considerations and proof-of-concept', *Limnology and Oceanography: Methods*, 19(8), pp. 497–509. doi: <https://doi.org/10.1002/lom3.10440>.

Jacox, M. G. *et al.* (2018) 'Coastal Upwelling Revisited: Ekman, Bakun, and Improved Upwelling Indices for the U.S. West Coast', *Journal of Geophysical Research: Oceans*, 123(10), pp. 7332–7350. doi: <https://doi.org/10.1029/2018JC014187>.

King, A. L. and Barbeau, K. A. (2011) 'Dissolved iron and macronutrient distributions in the southern California Current System', *Journal of Geophysical Research: Oceans*, 116(C3). doi: <https://doi.org/10.1029/2010JC006324>.

940 Knap, A. *et al.* (1996) 'Protocols for the Joint Global Ocean Flux Study (JGFOFS) Core Measurements', *JGOFS Reoprt Nr. 19, vi+170 pp*, (Reprint of IOC MAnuals and Guides 29, UNESCO 1994), p. 198.



950 Kolber, Z. and Falkowski, P. G. (1993) 'Use of active fluorescence to estimate phytoplankton photosynthesis in situ', *Limnology and Oceanography*, 38(8), pp. 1646–1665. doi: 10.4319/lo.1993.38.8.1646.

955 Kolber, Z. S., Prášil, O. and Falkowski, P. G. (1998) 'Measurements of variable chlorophyll fluorescence using fast repetition rate techniques: Defining methodology and experimental protocols', *Biochimica et Biophysica Acta - Bioenergetics*, 1367(1–3), pp. 88–106. doi: 10.1016/S0005-2728(98)00135-2.

Kranz, S. A. *et al.* (2020) 'Lagrangian Studies of Marine Production: A Multimethod Assessment of Productivity Relationships in the California Current Ecosystem Upwelling Region', *Journal of Geophysical Research: Oceans*, 125(6), p. e2019JC015984. doi: <https://doi.org/10.1029/2019JC015984>.

960 Lampe, R. H. *et al.* (2018) 'Different iron storage strategies among bloom-forming diatoms.', *Proceedings of the National Academy of Sciences of the United States of America*. United States, 115(52), pp. E12275–E12284. doi: 10.1073/pnas.1805243115.

965 Li, W. and Godzik, A. (2006) 'Cd-hit: a fast program for clustering and comparing large sets of protein or nucleotide sequences', *Bioinformatics*, 22(13), pp. 1658–1659. doi: 10.1093/bioinformatics/btl158.

Li, Z. *et al.* (2021) 'Dynamic Photophysiological Stress Response of a Model Diatom to Ten Environmental Stresses', *Journal of Phycology*, 57(2), pp. 484–495. doi: <https://doi.org/10.1111/jpy.13072>.

970 Lohan, M. C., Aguilar-Islas, A. M. and Bruland, K. W. (2006) 'Direct determination of iron in acidified (pH 1.7) seawater samples by flow injection analysis with catalytic spectrophotometric detection: Application and intercomparison', *Limnology and Oceanography: Methods*, 4(6), pp. 164–171. doi: <https://doi.org/10.4319/lom.2006.4.164>.

975 Love, M. I., Huber, W. and Anders, S. (2014) 'Moderated estimation of fold change and dispersion for RNA-seq data with DESeq2', *Genome Biology*, 15(12), p. 550. doi: 10.1186/s13059-014-0550-8.

Lund, J. W. G., Kipling, C. and Le Cren, E. D. (1958) 'The inverted microscope method of estimating algal numbers and the statistical basis of estimations by counting', *Hydrobiologia*, 11(2), pp. 143–170. doi: 10.1007/BF00007865.

980 M. Franck, V. *et al.* (2000) 'Iron and silicic acid concentrations regulate Si uptake north and south of the Polar Frontal Zone in the Pacific Sector of the Southern Ocean', *Deep Sea Research Part II: Topical Studies in Oceanography*, 47(15), pp. 3315–3338. doi: [https://doi.org/10.1016/S0967-0645\(00\)00070-9](https://doi.org/10.1016/S0967-0645(00)00070-9).

985 Marchetti, A. *et al.* (2017) 'Development of a molecular-based index for assessing iron status in bloom-forming pennate diatoms', *Journal of Phycology*, 53(4), pp. 820–832. doi: <https://doi.org/10.1111/jpy.12539>.

Marshak, A. R. and Link, J. S. (2021) 'Primary production ultimately limits fisheries economic performance', *Scientific Reports*, 11(1), p. 12154. doi: 10.1038/s41598-021-91599-0.

990 Martin, M. (2011) 'Cutadapt removes adapter sequences from high-throughput sequencing reads', *EMBnet.journal [Online]*, (17.1), pp. 10–12. doi: <https://doi.org/10.14806/ej.17.1.200>.

Mathis, M. *et al.* (2024) 'Enhanced CO₂ uptake of the coastal ocean is dominated by biological carbon fixation', *Nature Climate Change*. Springer US, 14(4), pp. 373–379. doi: 10.1038/s41558-024-01956-w.

995 McKew, B. A. *et al.* (2013) 'The trade-off between the light-harvesting and photoprotective functions of fucoxanthin-chlorophyll proteins dominates light acclimation in *Emiliania huxleyi* (clone CCMP 1516)', *New Phytologist*, 200(1), pp. 74–85. doi: <https://doi.org/10.1111/nph.12373>.



1000 Menard, H. W. and Dietz, R. S. (1952) 'Mendocino Submarine Escarpment', *The Journal of Geology*, 60(3), pp. 266–278. doi: 10.1086/625962.

1005 Mistry, J. *et al.* (2021) 'Pfam: The protein families database in 2021', *Nucleic Acids Research*, 49(D1), pp. D412–D419. doi: 10.1093/nar/gkaa913.

1005 Müller, P., Li, X. P. and Niyogi, K. K. (2001) 'Non-photochemical quenching. A response to excess light energy', *Plant Physiology*, 125(4), pp. 1558–1566. doi: 10.1104/pp.125.4.1558.

1010 Murphy, C. D. *et al.* (2017) 'Quantitating active photosystem II reaction center content from fluorescence induction transients', *Limnology and Oceanography: Methods*, 15(1), pp. 54–69. doi: 10.1002/lom3.10142.

1015 Niebergall, A. K. *et al.* (2023) 'Evaluation of new and net community production estimates by multiple ship-based and autonomous observations in the Northeast Pacific Ocean', *Elementa: Science of the Anthropocene*, 11(1), p. 107. doi: 10.1525/elementa.2021.00107.

1020 Olson, R. J. (1981) 'Differential photoinhibition of marine nitrifying bacteria: A possible mechanism for the formation of the primary nitrite maximum', *Journal of Marine Research*, 39. Available at: https://elischolar.library.yale.edu/journal_of_marine_research/1541.

1025 Oxborough, K. *et al.* (2012) 'Direct estimation of functional PSII reaction center concentration and PSII electron flux on a volume basis: A new approach to the analysis of Fast Repetition Rate fluorometry (FRRF) data', *Limnology and Oceanography: Methods*, 10(MARCH), pp. 142–154. doi: 10.4319/lom.2012.10.142.

1030 Patro, R. *et al.* (2017) 'Salmon provides fast and bias-aware quantification of transcript expression', *Nature Methods*, 14(4), pp. 417–419. doi: 10.1038/nmeth.4197.

1035 Pauly, D. and Christensen, V. (1995) 'Primary production required to sustain global fisheries', *Nature*, 374(6519), pp. 255–257. doi: 10.1038/374255a0.

1040 Pinckney, J. L. *et al.* (2001) 'Application of photopigment biomarkers for quantifying microalgal community composition and in situ growth rates', *Organic Geochemistry*, 32(4), pp. 585–595. doi: [https://doi.org/10.1016/S0146-6380\(00\)00196-0](https://doi.org/10.1016/S0146-6380(00)00196-0).

1045 Platt, T., Gallegos, C. L. and Harrison, W. G. (1980) 'Photo inhibition of photosynthesis in natural assemblages of marine phytoplankton', in.

1050 Raven, J. A., Evans, M. C. W. and Korb, R. E. (1999) 'The role of trace metals in photosynthetic electron transport in O₂ - evolving organisms', pp. 111–149.

1055 Roncel, M. *et al.* (2016) 'Iron deficiency induces a partial inhibition of the photosynthetic electron transport and a high sensitivity to light in the diatom *Phaeodactylum tricornutum*', *Frontiers in Plant Science*, 7(AUG2016), pp. 1–14. doi: 10.3389/fpls.2016.01050.

1060 Ryan-keogh, T. J. *et al.* (2020) 'Deriving a Proxy for Iron Limitation From Chlorophyll Fluorescence on Buoyancy Gliders', 7(May), pp. 1–13. doi: 10.3389/fmars.2020.00275.

1065 Saba, V. S. *et al.* (2011) 'An evaluation of ocean color model estimates of marine primary productivity in coastal and pelagic regions across the globe', pp. 489–503. doi: 10.5194/bg-8-489-2011.

1070 Sarthou, G. *et al.* (2005) 'Growth physiology and fate of diatoms in the ocean: a review', *Journal of Sea Research*, 53(1), pp.



25–42. doi: <https://doi.org/10.1016/j.seares.2004.01.007>.

1050

Schallenberg, C. *et al.* (2020) ‘Diel quenching of Southern Ocean phytoplankton fluorescence is related to iron limitation’, pp. 793–812.

1055

Schuback, N., Schallenberg, C., Duckham, C. and Maldonado, M. T. (2015) ‘Interacting Effects of Light and Iron Availability on the Coupling of Photosynthetic Electron Transport and CO₂ -Assimilation in Marine Phytoplankton’, *PLoS ONE*, pp. 1–30. doi: 10.1371/journal.pone.0133235.

1060

Schuback, N. *et al.* (2016) ‘Diurnal variation in the coupling of photosynthetic electron transport and Diurnal variation in the coupling of photosynthetic electron transport and carbon fixation in iron-limited phytoplankton in the NE subarctic Pacific’, (March). doi: 10.5194/bg-13-1019-2016.

Schuback, N. *et al.* (2017) ‘Primary productivity and the coupling of photosynthetic electron transport and carbon fixation in the Arctic Ocean’, *Limnology and Oceanography*, 62(3), pp. 898–921. doi: 10.1002/lo.10475.

1065

Schuback, N., Tortell, Philippe D, *et al.* (2021) ‘Single-Turnover Variable Chlorophyll Fluorescence as a Tool for Assessing Phytoplankton Photosynthesis and Primary Productivity: Opportunities, Caveats and Recommendations’, *Frontiers in Marine Science*, 8, p. 895. doi: 10.3389/fmars.2021.690607.

1070

Schuback, N. and Tortell, P. D. (2019) ‘Diurnal regulation of photosynthetic light absorption, electron transport and carbon fixation in two contrasting oceanic environments’, *Biogeosciences Discussions*, pp. 1–33. doi: 10.5194/bg-2018-524.

Schuler, K. H. and Tortell, P. D. (2023) ‘Impacts of vertical mixing and ice-melt on N₂O and CH₄ concentrations in the Canadian Arctic Ocean’, *Continental Shelf Research*, 269, p. 105124. doi: <https://doi.org/10.1016/j.csr.2023.105124>.

1075

Sezginer, Y. *et al.* (2021) ‘Irradiance and nutrient-dependent effects on photosynthetic electron transport in Arctic phytoplankton: A comparison of two chlorophyll fluorescence-based approaches to derive primary photochemistry’, *PLoS ONE*, 16(12 December), pp. 1–23. doi: 10.1371/journal.pone.0256410.

1080

Sezginer, Y. *et al.* (2023) ‘Fluorescence-based primary productivity estimates are influenced by non-photochemical quenching dynamics in Arctic phytoplankton’, *Frontiers in Microbiology*, 14. doi: 10.3389/fmicb.2023.1294521.

Smith, J. M. *et al.* (2014) ‘Differential contributions of archaeal ammonia oxidizer ecotypes to nitrification in coastal surface waters’, *The ISME Journal*, 8(8), pp. 1704–1714. doi: 10.1038/ismej.2014.11.

1085

Soneson, C., Love, M. I. and Robinson, M. D. (2016) ‘Differential analyses for RNA-seq: transcript-level estimates improve gene-level inferences [version 2; peer review: 2 approved]’, *F1000Research*, 4(1521). doi: 10.12688/f1000research.7563.2.

Spigai, J. J. (1971) *Marine geology of the continental margin off southern Oregon*. Oregon State University.

1090

Stanley, R. H. R. *et al.* (2010) ‘Net community production and gross primary production rates in the western equatorial Pacific’, *Global Biogeochemical Cycles*, 24(4). doi: <https://doi.org/10.1029/2009GB003651>.

Suggett D, Moore M, G. R. J. (2010) ‘Estimating Aquatic Productivity from Active Fluorescence Measurements’.

Suggett, D. J., Moore, C. M. and Geider, R. J. (2011) ‘Chlorophyll a fluorescence in Aquatic Sciences: Methods and Applications’, *Developments in Applied Phycology*.

1095

Sunda, W. G. and Huntsman, S. A. (1997) ‘Interrelated influence of iron, light and cell size on marine phytoplankton growth’, *Nature*, 390(6658), pp. 389–392. doi: 10.1038/37093.



1100 Suorsa, M. (2015) 'Cyclic electron flow provides acclimatory plasticity for the photosynthetic machinery under various environmental conditions and developmental stages', *Frontiers in Plant Science*, 6(September), pp. 1–8. doi: 10.3389/fpls.2015.00800.

1105 Till, C. P. *et al.* (2019) 'The iron limitation mosaic in the California Current System: Factors governing Fe availability in the shelf/near-shelf region', *Limnology and Oceanography*, 64(1), pp. 109–123. doi: <https://doi.org/10.1002/lo.11022>.

1110 Tortell, P. D., Schuback, N. and Suggett, D. J. (2023) *Application of Single Turnover Active Chlorophyll Fluorescence for Phytoplankton Productivity Measurements*. 2.0. doi: <http://dx.doi.org/10.25607/OPB-1084>.

1115 Tyrrell, T. and Law, C. S. (1997) 'Low nitrate:phosphate ratios in the global ocean', *Nature*, 387(6635), pp. 793–796. doi: 10.1038/42915.

1120 Wang, S. *et al.* (2020) 'Lagrangian Studies of Net Community Production: The Effect of Diel and Multiday Nonsteady State Factors and Vertical Fluxes on O₂/Ar in a Dynamic Upwelling Region', *Journal of Geophysical Research: Biogeosciences*, 125(6), p. e2019JG005569. doi: <https://doi.org/10.1029/2019JG005569>.

Xu, K. *et al.* (2018) 'Phytoplankton σPSII and excitation dissipation; Implications for estimates of primary productivity', *Frontiers in Marine Science*, 5(AUG). doi: 10.3389/fmars.2018.00281.

Zhu, Y. *et al.* (2017) 'Relationship between light, community composition and the electron requirement for carbon fixation in natural phytoplankton', *Marine Ecology Progress Series*, 580, pp. 83–100. doi: 10.3354/meps12310.